# EVALUATION OF LASER-BASED OXIDE REMOVAL AS AN ALTERNATIVE TO ACID PICKLING IN CONTINUOUS FLAT STEEL PROCESSING LINES: ENERGY CONSUMPTION AND GREEN TRANSITION PERSPECTIVE

A THESIS SUBMITTED TO
THE GRADUATE SCHOOL OF NATURAL AND APPLIED SCIENCES
OF
MIDDLE EAST TECHNICAL UNIVERSITY

BY

EREN ÇELİKSES

IN PARTIAL FULFILLMENT OF THE REQUIREMENTS
FOR
THE DEGREE OF MASTER OF SCIENCE
IN
METALLURGICAL AND MATERIALS ENGINEERING

APRIL 2026

Approval of the thesis:

**EVALUATION OF LASER-BASED OXIDE REMOVAL AS AN ALTERNATIVE TO ACID PICKLING IN CONTINUOUS FLAT STEEL PROCESSING LINES: ENERGY CONSUMPTION AND GREEN TRANSITION PERSPECTIVE**

submitted by **EREN ÇELİKSES** in partial fulfillment of the requirements for the degree of **Master of Science** i**n Metallurgical and Materials Engineering, Middle East Technical University** by,

Prof. Dr. Naci Emre Altun
Dean, **Graduate School of Natural and Applied Sciences** _____

Prof. Dr. Kadri Aydınol
Head of the Department, **Metallurgical and Materials Engineering** _____

Assist. Prof. Dr. İrem Nur Gamze Özbilgin
Supervisor, **Metallurgical and Materials Engineering, METU** _____

**Examining Committee Members:**

Prof. Dr. Bilgehan Ögel
Metallurgical and Materials Eng, METU _____

Assist. Prof. Dr. İrem Nur Gamze Özbilgin
Metallurgical and Materials Eng, METU _____

Prof. Dr. Cevdet Kaynak
Metallurgical and Materials Eng, METU _____

Assist. Prof. Dr. İrem Burcu Algan Şimşek
Metallurgical and Materials Eng, Gazi University _____

Assist. Prof. Dr. Yusuf Keleştemur
Metallurgical and Materials Eng, METU _____

Date: 20.04.2026

**I hereby declare that all information in this document has been obtained and presented in accordance with academic rules and ethical conduct. I also declare that, as required by these rules and conduct, I have fully cited and referenced all material and results that are not original to this work.**

Name Last name : Çelikses Eren

Signature :

# ABSTRACT

## EVALUATION OF LASER-BASED OXIDE REMOVAL AS AN ALTERNATIVE TO ACID PICKLING IN CONTINUOUS FLAT STEEL PROCESSING LINES: ENERGY CONSUMPTION AND GREEN TRANSITION PERSPECTIVE

Çelikses Eren
Master of Science, Metallurgical and Materials Engineering
Supervisor: Assist. Prof. Dr. İrem Nur Gamze Özbilgin

April 2026, 73 pages

The steel industry's transition towards decarbonization necessitates sustainable alternatives to conventional, energy-intensive, and environmentally hazardous hydrochloric acid pickling processes. Laser-based descaling has emerged as a promising chemical-free surface preparation technology; however, its industrial-scale integration for hot-rolled flat steels is hindered by the complex, multi-layered nature of oxide layer (wüstite, magnetite, and hematite) and a lack of comprehensive economic feasibility studies. This thesis systematically investigates the feasibility and operational efficiency of employing a 1070 nm fiber laser for descaling hot-rolled flat steels. The study employs a multi-stage methodology, beginning with the microstructural and morphological characterization of the oxide layer, including thickness variation analysis and phase distribution mapping via Electron Backscatter Diffraction (EBSD). Subsequently, UV-Vis-NIR spectroscopy is utilized to determine the phase-dependent optical absorption characteristics, providing a scientific basis for optimal laser interaction. A rigorous parametric experimental study is then conducted using both Continuous-Wave (CW) and Pulsed-Wave (PW) laser modes to evaluate ablation efficiency, monitor phase transformations, and define the optimal operational window. Finally, the research correlates the achieved

laser cleaning speeds with energy consumption metrics to perform a comparative industrial feasibility analysis against conventional Continuous Pickling Lines (CPL). Additionally, comparative surface integrity analyses revealed that the selected laser-cleaning parameters resulted in higher surface roughness, a laser-affected near-surface region of approximately 10–22 μm, and localized hardness increase compared with conventional pickling, highlighting the need for further parameter optimization, particularly for products subjected to subsequent cold rolling. Ultimately, this study aims to provide a robust scientific and economic foundation for the implementation of laser descaling technology in modern, high-speed steel production lines, contributing significantly to the industry's green transition initiatives.

Keywords: Flat Steel Production, Hot-Rolled Steel Oxide Scale Characterization, Laser-based Oxide Removal, Carbon Footprint Assessment, Green Transition

# ÖZ

## SÜREKLİ YASSI ÇELİK İŞLEME HATLARINDA ASİTLE TEMİZLEMEYE ALTERNATİF OLARAK LAZER TABANLI OKSİT GİDERİMİNİN DEĞERLENDİRİLMESİ: ENERJİ TÜKETİMİ VE YEŞİL DÖNÜŞÜM PERSPEKTİFİ

Çelikses Eren
Yüksek Lisans, Metalurji ve Malzeme Mühendisliği
Tez Yöneticisi: Dr. Öğr. Üy. İrem Nur Gamze Özbilgin

Nisan 2026, 73 sayfa

Çelik endüstrisinin karbonsuzlaşma hedefleri, enerji yoğun ve çevreye zararlı geleneksel hidroklorik asit dekapaj işlemlerine sürdürülebilir alternatifler bulunmasını zorunlu kılmaktadır. Lazer tabanlı tufal giderme teknolojisi, kimyasal içermeyen yenilikçi bir yüzey hazırlama yöntemi olarak öne çıkmaktadır; ancak sıcak haddelenmiş yassı çelikler için endüstriyel ölçekte entegrasyonu, oksit tabakasının karmaşık, çok katmanlı yapısı (wüstit, manyetit ve hematit) ve kapsamlı ekonomik fizibilite çalışmalarının eksikliği nedeniyle henüz sınırlıdır. Bu tez, sıcak haddelenmiş yassı çeliklerin temizlenmesinde 1070 nm fiber lazer kullanımının uygulanabilirliğini ve operasyonel verimliliğini sistematik olarak incelemektedir. Çalışma; tufal tabakasının kalınlık varyasyonu analizini ve Elektron Geri Saçılım Kırınımı (EBSD) ile faz dağılımının haritalandırılmasını içeren mikroyapısal ve morfolojik karakterizasyon ile başlayan çok aşamalı bir metodoloji benimsemektedir. Ardından, faza bağlı optik soğurma özelliklerini belirlemek ve optimum lazer etkileşimi için temel oluşturmak amacıyla UV-Vis-NIR spektroskopisi kullanılmıştır. Ablasyon verimliliğini değerlendirmek, faz dönüşümlerini izlemek ve optimum operasyonel parametre penceresini tanımlamak için hem Sürekli Dalga (CW) hem de Darbeli (PW) lazer modlarında kapsamlı

deneysel çalışmalar yürütülmüştür. Son olarak, elde edilen lazer temizleme hızları enerji tüketim metrikleriyle ilişkilendirilerek, geleneksel Sürekli Dekapaj Hatlarına (CPL) kıyasla endüstriyel bir fizibilite ve maliyet analizi gerçekleştirilmiştir. Ek olarak, yüzey bütünlüğü analizleri lazer temizlemenin daha yüksek yüzey pürüzlülüğüne, yüzeye yakın bölgede mikroyapısal değişime ve lokal sertlik artışına neden olabileceğini göstermiştir. Bu bulgular, özellikle sonraki aşamada soğuk haddeleme işlemine tabi tutulacak ürünler için, endüstriyel uygulama öncesinde lazer parametrelerinin daha ileri düzeyde optimize edilmesi gerektiğini ortaya koymaktadır. Nihayetinde bu çalışma, lazerle tufal temizleme teknolojisinin modern ve yüksek hızlı çelik üretim hatlarına entegrasyonu için sağlam bir bilimsel ve ekonomik zemin oluşturmayı ve sektörün yeşil dönüşümüne katkı sağlamayı amaçlamaktadır.

Anahtar Kelimeler: Yassı Çelik Üretimi, Sıcak Haddelenmiş Çelik Oksit Tabakası Karakterizasyonu, Lazer Tabanlı Oksit Giderme, Karbon Ayak İzi Değerlendirmesi, Yeşil Dönüşüm

To the memory of those who lost their lives in the school attack in Kahramanmaraş on April 15, 2026, with deep respect:

*Almina Ağaoğlu*

*Ayla Kara*

*Adnan Göktürk Yeşil*

*Bayram Nabi Şişik*

*Belinay Nur Boyraz*

*Furkan Sancak Balal*

*Kağan Güngör*

*Kerem Erdem Güngör*

*Şuranur Sevgi Kazıcı*

*Yılmaz Efe Konar*

*Yusuf Tarık Gül*

*Zeynep Kılıç*

## ACKNOWLEDGMENTS

This thesis has been a long and challenging journey, initially starting with the micromechanical modeling of dual-phase steels. Tragically, I was deeply saddened by the passing of my esteemed advisor, Assoc. Prof. Dr. Caner Şimşir. I respectfully wish him Allah's mercy.

Following his loss, I restructured my Borçelik project on laser-based surface cleaning technologies into a more comprehensive framework for this thesis. I sincerely thank my advisor, Asst. Prof. Dr. İrem Nur Gamze Özbilgin. She guided me on this new path, helped interpret the most incomprehensible test results, directed me in selecting the right experiments, and supported me whenever I was stuck.

Deep gratitude to Celal Seyalıoğlu and Baran Burat, who hold a very special place for me. They supported my education from day one, encouraging my weekly Bursa-Ankara travels. I also thank my manager Ozan Faik Tumba for financing my experiments and standing by me.

I am incredibly thankful to my leader Nurten Başak Dülger, who granted me immense peace of mind, simply saying, 'Just finish it, this is a top priority.' Thanks also to my colleague Emre Kocakuşaklı, with whom I worked shoulder to shoulder and who covered for me during this time, and to the R&D Test Center team—especially Ramazan Altın and Emre Dombaylı—for their devoted assistance.

Thank you to my dear friend Duygu İnce, who supported my entire education, whether by sharing lecture notes or literally ringing my doorbell to drag me to class.

Heartfelt thanks to my precious family—my father Ali Çelikses, mother Melahat Çelikses, and brother Efe Çelikses—for their unwavering support and always making me believe in myself.

Finally, I owe a massive debt of gratitude to my companion and my love, Özge Özel. She stood by me through the most exhausting moments, keeping me fueled with tea and coffee, comforting me in despair, and selflessly proofreading this completely foreign thesis multiple times just to catch typographical errors.

## TABLE OF CONTENTS

ABSTRACT ..... v

ÖZ ..... vii

ACKNOWLEDGMENTS ..... x

TABLE OF CONTENTS ..... xi

LIST OF TABLES ..... xiii

LIST OF FIGURES ..... xiv

1 INTRODUCTION ..... 1

2 LITERATURE REVIEW ..... 5

2.1 Steel ..... 5

2.1.1 Steel Production ..... 11

2.1.2 Green Transition in the Steel Industry ..... 22

2.1.3 Laser Descaling of Oxide Scales on Hot Rolled Steel Strip ..... 24

2.1.4 Scope and Objective of the Study ..... 26

3 CHARACTERIZATION OF OXIDE LAYER ON HOT-ROLLED FLAT STEEL ..... 29

3.1.1 Material Selection and Sampling Strategy ..... 30

3.1.2 Microstructural Analysis and Oxide Layer Thickness Measurement 32

3.2 Crystallographic Phase Analysis via Electron Backscatter Diffraction .. 38

3.3 Optical Property Characterization and Laser Source Selection ..... 43

4 EXPERIMENTAL INVESTIGATION OF LASER-BASED OXIDE REMOVAL ..... 47

4.1 Continuous-Wave (CW) Laser Cleaning Experiments ..... 50

4.2 Pulsed Wave Laser Cleaning Experiments ..... 51

5 INDUSTRIAL FEASIBILITY AND PERFORMANCE ANALYSIS ..... 56
5.1 Operational Comparison: Pickling vs. Laser Cleaning ..... 56
5.2 Energy Comparison Methodology and Decarbonization ..... 57
5.3 Comparative Surface Integrity Assessment of Pickled and Laser-Cleaned Steel ..... 58
6 CONCLUSIONS AND FUTURE RECOMMENDATIONS ..... 65
REFERENCES ..... 68

## LIST OF TABLES

TABLES

**Table 2-1** Properties according to TS-EN 10209 (Cold rolled low carbon steel flat products for vitreous enameling) ..... 10
**Table 3-1** Elemental composition (wt.%) and coiling temperature classifications of the experimental steel samples..... 32
**Table 3-2** Statistical summary of oxide scale thicknesses (mean, standard deviation, minimum, and maximum in μm) measured across the strip width (drive side, middle, and work side) for the investigated hot-rolled steel samples. ..... 35
**Table 3-3** Quantitative phase fractions of the oxide layers derived from EBSD analysis..... 42
**Table 4-1** Morphological evolution of the oxide scale (ablation stages) across the Pulsed-Wave (PW) experimental parameter matrix ..... 54
**Table 4-2** Successful PW Cleaning Parameters (Stage 4) and Energy Efficiency Metrics. ..... 55
**Table 5-1** Utility Consumption Comparison per Metric Ton of Steel. ..... 58
**Table 5-2** Surface roughness measurements of conventionally pickled and laser-cleaned steel samples. ..... 60

## LIST OF FIGURES

FIGURES

**Figure 2-1** Temperature-pressure phase diagram of pure iron illustrating the stability regions of ferrite (α), austenite (γ), delta-ferrite (δ), and epsilon-iron (ε) along with the liquid phase. ..... 6
**Figure 2-2** The Iron-Carbon (Fe-$Fe_3C$) metastable phase diagram, illustrating the stability regions of ferrite (α), austenite (γ), delta-ferrite (δ), cementite ($Fe_3C$), and intermediate structures like pearlite and ledeburite, as a function of temperature and carbon mass fraction. Critical temperatures (723°C, 768°C, 911°C, 1147°C, 1493°C, 1536°C) and key points are indicated. ..... 7
**Figure 2-3** Optical micrograph of DP780 steel at 1000x magnification (Light regions: Ferrite matrix, Dark regions: Martensite islands) ..... 9
**Figure 2-4** Steel production technologies and their total GHG emissions from 1900 to 2015. ..... 13
**Figure 2-5** Schematic comparison of conventional (BF-BOF), natural gas-based (DR-EAF), and hydrogen-based (H-DR-EAF) steelmaking routes. ..... 15
**Figure 2-6** Cross-sectional diagram of a blast furnace showing charge materials, slag formation, and the indirect/direct reduction zones. (Image generated by Gemini AI.) ..... 16
**Figure 2-7** Process Flow Diagram and Integrated Acid Regeneration Loop of the Borçelik Continuous Pickling Line (CPL). ..... 20
**Figure 3-1** A visualization of a flat-rolled steel strip, identifying key positional zones used for analysis. Leader lines clearly indicate the positions corresponding to the Drive Side (DS), Center (MID), and Working Side (WS) across the product width. (Image generated by Gemini AI.) ..... 33
**Figure 3-2** Cross-sectional SEM micrographs detailing the oxide scale thickness from the drive side (DS) of the hot-rolled CHI-1 sample. The panels (a–f) illustrate the local variation in scale thickness across different measurement regions (750x magnification, scale bar = 2 μm). ..... 34

**Figure 3-3** Cross-sectional EBSD phase maps revealing the oxide scale constitution and spatial phase distribution of the representative samples: (a) TUR-1 (standard baseline), (b) TUR-2 (high coiling temperature), (c) FRA-1 (high-carbon grade), and (d) KOR-1 (low-carbon grade). ..... 40
**Figure 3-4** High-resolution EBSD phase maps providing a detailed spatial distribution of the identified oxide phases (Hematite, Magnetite, and Wüstite) for the representative specimens: (a) TUR-1, (b) TUR-2, (c) FRA-1, and (d) KOR-1. 41
**Figure 3-6** UV-Vis-NIR Absorption Spectra of Oxide Phases ..... 44
**Figure 4-1** A photograph of the setup used for the experiments ..... 48
**Figure 4-2** Sample of a laser-exposed specimen ..... 49
**Figure 4-3** Cross-sectional SEM micrographs illustrating the morphological evolution of the oxide scale across the defined ablation stages under pulsed-wave (PW) laser irradiation. The panels sequentially demonstrate: (a) Stage 0, the initial intact mill scale; (b) Stage 1, crack initiation and localized superficial spallation; (c) Stage 2, partial ablation leaving un-ablated oxide islands; (d) Stage 3, a predominantly clean surface with trace interfacial residues; and (e) Stage 4, complete and uniform descaling exposing the bare metallic iron substrate without thermal damage. ..... 53

# CHAPTER 1

# INTRODUCTION

Steel remains one of the most fundamental materials in modern industrial society, underpinning infrastructure, transportation, energy systems, and manufacturing. Its widespread use is primarily attributed to its exceptional versatility, which arises from the ability to tailor its microstructure and properties through precise control of chemical composition and thermomechanical processing. This flexibility has enabled the development of a wide range of steel grades with application-specific performance characteristics, making steel indispensable across nearly all engineering disciplines.

Despite these advantages, the steel industry faces significant challenges in the context of environmental sustainability. Conventional steel production routes, particularly the blast furnace–basic oxygen furnace (BF–BOF) process, are highly energy-intensive and contribute substantially to global greenhouse gas emissions. In addition to upstream emissions, downstream processes such as surface preparation also involve considerable environmental burdens. Among these, acid pickling—widely used to remove oxide scale from hot-rolled steel—relies on aggressive chemical treatments, generates hazardous waste streams, and requires energy-intensive regeneration systems.

In response to these challenges, the steel industry is undergoing a transformative shift toward more sustainable production practices. While large-scale decarbonization strategies, such as hydrogen-based direct reduction, target primary production processes, increasing attention is being directed toward improving efficiency and reducing environmental impact in downstream operations. In this context, alternative surface treatment technologies that eliminate chemical usage and reduce energy consumption have become a critical area of research.

Laser-based descaling has emerged as a promising candidate to replace conventional pickling processes. Unlike chemical methods, laser descaling relies on a purely physical mechanism in which high-intensity laser radiation interacts with the oxide layer, leading to its removal through photothermal and thermomechanical effects. This approach offers several potential advantages, including the elimination of chemical waste, reduced environmental impact, and improved process controllability. However, the successful implementation of laser descaling in industrial applications requires a comprehensive understanding of the interaction between the laser beam and the oxide scale.

The oxide layer formed on hot-rolled steel is a complex, multi-phase structure consisting primarily of hematite ($Fe_2O_3$), magnetite ($Fe_3O_4$), and wüstite (FeO). The thickness, morphology, and phase distribution of this scale are highly sensitive to process parameters such as cooling rate, coiling temperature, and alloy composition. Since each oxide phase exhibits distinct optical and thermophysical properties, their presence directly influences the absorption of laser energy and the efficiency of the descaling process. Consequently, a one-size-fits-all approach to laser parameter selection is not feasible, and a material-specific optimization strategy is required.

Although numerous studies have investigated laser-based oxide removal, existing research predominantly focuses on laboratory-scale demonstrations and parameter optimization under controlled conditions. There remains a significant gap in understanding the industrial feasibility of laser descaling, particularly in terms of energy efficiency, process scalability, and its role within the broader context of sustainable steel production. In addition, the relationship between oxide layer characteristics and laser–material interaction has not been sufficiently quantified for real production materials exhibiting process-induced variability.

The primary objective of this thesis is to address these gaps by systematically evaluating laser-based descaling as a viable alternative to conventional pickling in hot-rolled flat steel production. This study focuses on three key aspects: (i) detailed characterization of the oxide layer in terms of morphology, phase composition, and

optical properties, (ii) experimental investigation of laser–oxide interaction and process parameter optimization, and (iii) assessment of industrial feasibility and performance analysis in comparison with conventional pickling processes.

By integrating materials characterization, process optimization, and energy analysis, this work aims to provide a comprehensive framework for the implementation of laser descaling in industrial environments. Ultimately, the findings contribute to the ongoing transition toward cleaner and more sustainable steel production technologies.

# CHAPTER 2

# LITERATURE REVIEW

## 2.1 Steel

Steel is an alloy, with iron as its primary constituent. A deep understanding of steel's properties, therefore, requires an understanding of the properties of the element iron. As the most abundant element by mass on Earth, iron (Fe) is a metal with a crystalline structure. It has an atomic number of 26 and a relative atomic mass of 55.85, commonly exhibits valence states of $2^+$ and $3^+$. It is not found in pure form in nature but exists in compounds with other elements, mainly as iron oxides such as hematite ($Fe_2O_3$) and magnetite ($Fe_3O_4$). [1]

The term "iron" primarily denotes to the element itself and, subsequently, to a material containing over 99.99% elemental Fe, with the remainder being impurities, as producing completely pure iron is exceedingly difficult. Iron exhibits allotropy, the ability to change its crystal lattice structure with temperature and pressure. The primary allotropes are body-centered cubic (α-iron) and face-centered cubic (γ-iron) [2]. At room temperature and up to 911 °C, iron is in its α-iron form also called ferrite. At 911 °C, it rapidly transforms into the γ-iron structure. At 1392 °C, the lattice reverts to an α-form (designated as δ-iron) before melting at 1536 °C. It is also worth noting that under high pressure, a hexagonal close-packed (HCP) ε-iron phase can form, which is a key consideration in planetary science and high-pressure materials research [2]. This behavior is best visualized in a temperature-pressure phase diagram, shown in Figure 2.1.

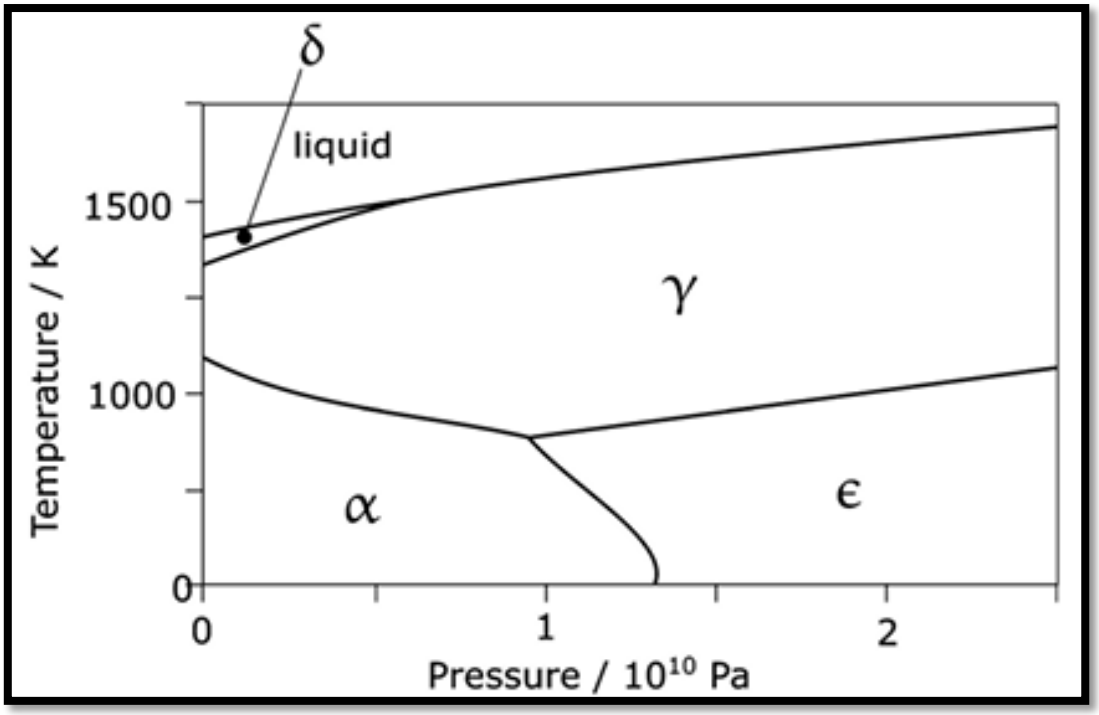


**Figure 2-1** Temperature-pressure phase diagram of pure iron illustrating the stability regions of ferrite (α), austenite (γ), delta-ferrite (δ), and epsilon-iron (ε) along with the liquid phase.

Steel is an alloy of iron with other elements, most importantly carbon, as well as non-metals like silicon, phosphorus, and sulfur, and metals such as manganese, chromium, and nickel. In steel, unlike pure iron, these alloying elements are incorporated into the lattice in several ways. Elements with similar atomic radii, such as chromium, form a substitutional solid solution by replacing iron atoms within the lattice. Alternatively, small-radius elements like carbon occupy the interstitial spaces between the iron atoms, forming an interstitial solid solution. Some elements also combine with iron to form distinct compounds, such as iron carbide ($Fe_3C$), also known as cementite [3]. The presence of these alloying elements significantly influences the material's mechanical, corrosion, and electrical behaviors by altering the lattice structure, thereby allowing for the precise control of specific performance characteristics. While the iron-carbon phase diagram below illustrates the fundamental effects of carbon on phases, it is important to note that it only represents

a simplified binary system. In practice, modern steel design involves a much more complex process where multiple alloying elements are added to achieve specific microstructures and material properties tailored for various applications. Through careful chemical design, material engineers have been able to produce a wide range of steels to meet diverse industrial needs [4].

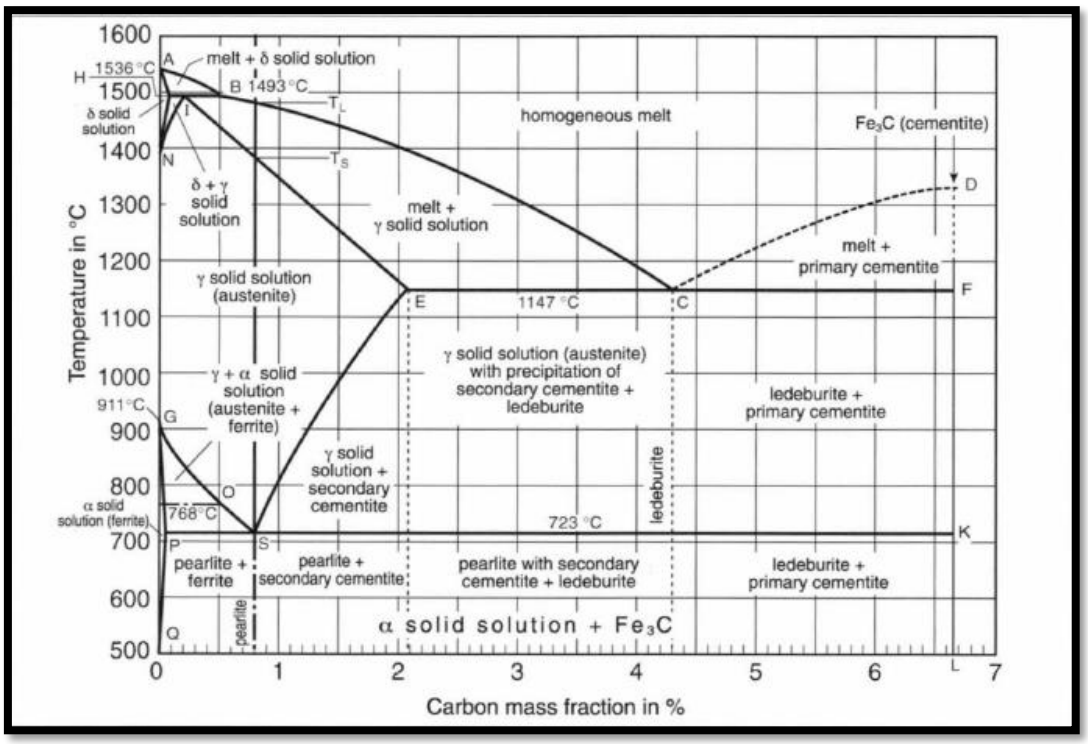


**Figure 2-2** The Iron-Carbon (Fe-$Fe_3C$) metastable phase diagram, illustrating the stability regions of ferrite (α), austenite (γ), delta-ferrite (δ), cementite ($Fe_3C$), and intermediate structures like pearlite and ledeburite, as a function of temperature and carbon mass fraction. Critical temperatures (723°C, 768°C, 911°C, 1147°C, 1493°C, 1536°C) and key points are indicated.

Historically, the defining characteristic of steel was its hardenability. However, this definition is no longer universally applicable. Modern standards, such as those set by Euronorm 1 and EN 10020, now define steel as a ferrous material where the iron mass fraction is the highest among all elements. It is distinguished from cast iron by a maximum carbon content of 2%, with some exceptions in high-chromium grades.

Although chemical composition forms the basis for defining steel, it is not sufficient to characterize its properties. The same composition can result in vastly different mechanical behaviors depending on the microstructure. Therefore, heat treatment plays a critical role by enabling precise control over the microstructure and, consequently, the performance of steels [5]. This principle forms the basis of heat treatments used to control the steel's microstructure and mechanical properties. For example, pearlite, which forms during slow cooling, is a layered structure composed of ferrite and cementite. As the cooling rate increases, the distance between these layers decreases, and the steel becomes harder and more resistant. If the cooling rate is sufficiently high, pearlite formation is suppressed due to the limited diffusion of carbon. Under these conditions, carbon atoms become trapped within the austenite lattice, leading to the formation of martensite. This represents a typical example of microstructural design in steels achieved through heat treatment. In industrial practice, steels generally consist of phases such as ferrite, pearlite, bainite, martensite, (retained) austenite, and cementite, and their distribution, volume fraction, and chemical composition collectively govern the resulting material properties [6].

As an example, Dual-Phase (DP) steels are considered one of the most significant developments in modern materials engineering, offering a unique combination of high strength and good ductility [7][8]. These materials provide an excellent illustration of how microstructure can be precisely engineered through heat treatment. Unlike conventional approaches, DP steels are produced using a specialized method known as intercritical annealing, where the material is heated into the intercritical ($\alpha + \gamma$) region and then cooled at a controlled cooling rate tailored to promote partial martensitic transformation [9]. This process results in a characteristic microstructure consisting of hard martensite islands dispersed within a soft and ductile ferrite matrix. This microstructural configuration provides DP steels with a unique mechanical properties, making them particularly attractive for advanced structural applications.

**Figure 2-3** Optical micrograph of DP780 steel at 1000x magnification (Light regions: Ferrite matrix, Dark regions: Martensite islands)

Beyond chemical composition and heat treatment, steel properties are also influenced by factors such as phase morphology, grain size, and defects. In modern materials engineering, this complexity is further expanded through advanced surface treatments and innovative coating technologies. These developments enable the design of steels with highly tailored and application-specific properties, significantly broadening the achievable performance range. However, this increasing diversity in microstructures and properties has made standardization essential for the consistent definition and classification of steels [10]. To ensure consistency, reliability, and safety across various applications, the chemical and mechanical properties of steels, as well as their dimensional tolerances, are strictly defined by a comprehensive set of standards. This process is governed by a range of international, regional, and national organizations. Key international bodies include the International Organization for Standardization (ISO), while regionally, the European Committee

for Standardization (CEN) and the American Society for Testing and Materials (ASTM) are among the most influential [10]. Nationally, organizations like the Turkish Standards Institution (TSE) adopt and implement these standards, ensuring local compliance.

These standards extend beyond defining fundamental properties to ensure product consistency and quality. For example, the TS EN 10209 standard, which specifies requirements for cold-rolled low-carbon flat steel products intended for vitreous enamelling, defines not only chemical composition and mechanical properties but also regulates physical and geometrical characteristics, such as thickness and width tolerances of the coil. The table below presents the specified chemical and mechanical property limits for different steel grades according to TS EN 10209. The use of such standardized designations enables manufacturers to procure equivalent materials from different suppliers without redefining detailed specifications, thereby ensuring consistency and interchangeability across the supply chain.

**Table 2-1** Properties according to TS-EN 10209 (Cold rolled low carbon steel flat products for vitreous enameling)

| **EN 10027-1** | ***Mechanical Properties*** | | | ***Chemical Composition (ladle analysis) %max*** | | | | |
|---|---|---|---|---|---|---|---|---|
| **Designation** | $R_{p\ max\ (MPa)}$ | $R_{m\ (MPa)}$ | $A_{80\ \%min}$ | ***C*** | ***Ti*** | ***Mn*** | ***P*** | ***S*** |
| **DC01EK** | 270 | 270-390 | 270-390 | 0.08 | | 0.60 | 0.045 | 0.05 |
| **DC04EK** | 220 | 270-350 | 270-350 | 0.08 | | 0.50 | 0.025 | 0.05 |
| **DC06EK** | 190 | 270-350 | 270-350 | 0.02 | 0.3 | 0.50 | 0.020 | 0.05 |
| **DC04ED** | 210 | 270-350 | 270-350 | 0.004 | | 0.40 | 0..30 | 0.05 |
| **DC06ED** | 190 | 270-350 | 270-350 | 0.02 | 0.3 | 0.34 | 0.020 | 0.05 |

This widespread reliance on standardized steel grades highlights the material's critical role in modern industry. Although the steel industry is often perceived as a "dirty" sector due to its high carbon emissions, steel is also one of the most recyclable materials available [11]. Owing to its wide range of properties and high recyclability, it constitutes a cornerstone of sustainable development in modern industrial

societies. Its applications are extensive, spanning nearly every engineering discipline—from machinery and equipment manufacturing to civil infrastructure, energy production, environmental technologies, and transportation.

Steel distinguishes itself among engineering materials through its exceptional versatility, adaptability, and cost-effectiveness. In terms of economic advantages, the energy required to produce iron from ore is significantly lower than that needed for many other primary metals [12]. Beyond these economic merits, the widespread use of steel is primarily driven by its outstanding technical properties. These include its high formability for both hot and cold forming processes, excellent weldability in joining operations, and favorable machinability for manufacturing. Furthermore, steel offers superior mechanical integrity, encompassing high hardness, ductility, and wear resistance, along with impressive corrosion resistance and reliable high-temperature performance against creep and deformation [13].

Given the enormous production volume of the steel industry, even incremental improvements can have a disproportionately large global impact. Decarbonization efforts in this field are advancing rapidly, with numerous projects and international initiatives currently underway. Consequently, focusing on this sector and seeking innovative solutions to reduce its carbon emissions represents a realistic and highly impactful research direction [14][15]. In this study, particular emphasis is placed on steel production processes, which are examined in greater detail to facilitate a deeper understanding of their role in sustainability transitions.

### 2.1.1 Steel Production

The production of iron and steel has profoundly shaped human civilization for millennia. Following the Stone and Bronze Ages, the Iron Age began when humanity mastered the techniques to smelt and forge iron from naturally occurring ores. Early blacksmiths produced a porous mass known as sponge iron in simple bloomery furnaces. This material was then repeatedly hammered to expel impurities and shape

it into usable tools. Although these early techniques were primitive, they laid the foundation for one of the most transformative materials in history[16].

Iron's versatility extended beyond its structural applications, establishing it as a symbol of power. From agricultural implements that revolutionized farming to weapons that redefined warfare, the widespread use of iron became a defining characteristic of ancient societies. The production of iron swords, spears, and armor during antiquity underscores its profound cultural and military impact. Legendary examples, such as Damascus steel blades and Japanese katanas, demonstrate an early understanding of how to control carbon content through sophisticated forging and folding techniques—principles that remain central to modern steel metallurgy [17].

With the onset of the Industrial Revolution, steelmaking entered a new era. The invention of the Bessemer converter in 1856 enabled large-scale steel production by blowing pressurized air through molten pig iron, which drastically reduced production costs. This innovation was soon followed by the Siemens-Martin open-hearth furnace, a process that dominated global steel production until the mid-20th century [18]. However, these energy-intensive methods were eventually superseded by more efficient modern processes. Today, ironmaking is primarily carried out through two major routes: the ore-based integrated production route and the scrap-based electric arc furnace route [19].

The integrated production route, which accounts for approximately 70–75% of global steel production, relies on a blast furnace (BF) followed by a basic oxygen furnace (BOF). In this method, iron ore is charged into the blast furnace along with coke. Carbon monoxide and hydrogen act as the primary reducing agents, converting iron oxides into metallic iron. The resulting hot metal is then refined in a BOF, where pure oxygen is blown into the melt to remove carbon and other impurities. The second primary method is the scrap-based electric arc furnace (EAF) route. In this process, scrap steel is melted in electric arc furnaces. While initially used for specialty and alloy steels, EAF technology is now capable of producing a wide range of steels, including low-carbon grades. This route offers a number of advantages,

including increased flexibility, lower capital investment, and reduced $CO_2$ emissions due to the use of recycled materials. However, the presence of tramp elements like Cu and Sn from the scrap can sometimes affect steel quality. To mitigate this, direct reduced iron (DRI) or hot briquetted iron (HBI) is often added to the EAF charge to enhance both quality and process stability.

The following chapters will delve into the details of these modern ironmaking and steelmaking processes. The overall modern steel production chain, illustrating the tonnages and flow between these various routes, is shown in Figure 2.4.

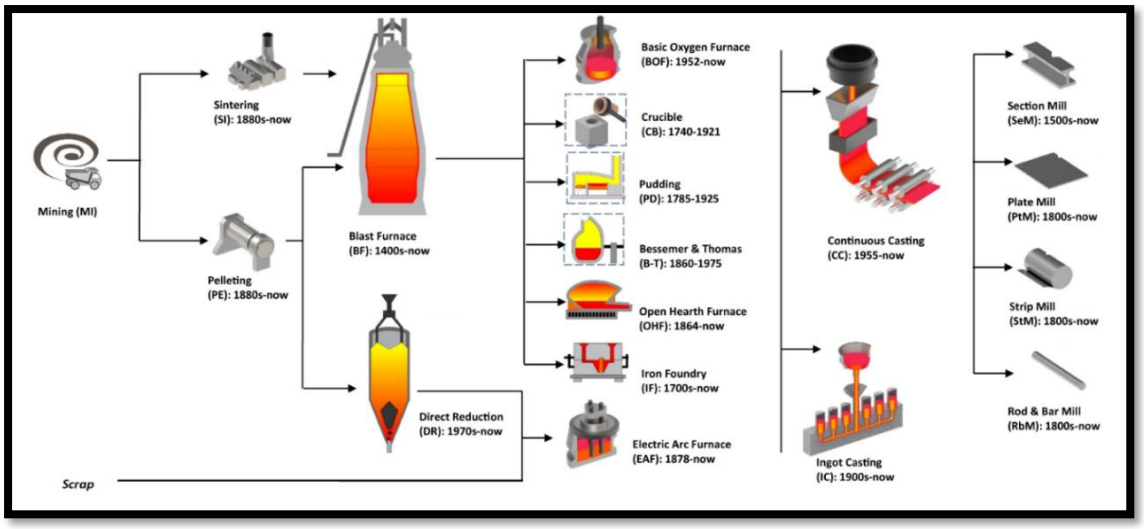


**Figure 2-4** Steel production technologies and their total GHG emissions from 1900 to 2015.

### 2.1.1.1 Raw Material Preparation

The raw materials used in iron and steel production must be subjected to pretreatment before being charged into furnaces. The main objectives of these pretreatments are to homogenize the chemical composition, optimize particle size and porosity to enhance gas–solid interactions, and ultimately improve furnace efficiency while reducing fuel consumption [13].

For the traditional integrated route (BF-BOF), the agglomeration of fine iron ores is critical. Sintering and pelletizing are the most common methods used to transform fine ores into physically strong, porous materials. These agglomerates are essential for maintaining adequate gas permeability within the blast furnace burden, accelerating the reduction kinetics, and lowering the overall energy demand.

Crucial to this integrated process is metallurgical coke. Produced by heating coking coal in the absence of oxygen, coke serves a dual function within the blast furnace: it acts as the primary source of thermal energy and as the chemical reducing agent for the iron oxides. Furthermore, its hard, porous structure provides the essential load-bearing framework that allows gases to flow freely through the massive burden of ore and flux—a critical mechanical requirement for efficient furnace operation [21].

In contrast, the Electric Arc Furnace (EAF) route relies on Direct Reduced Iron (DRI) as a high-quality feedstock, either complementing or replacing steel scrap. In DRI processes, iron oxides are reduced to metallic iron in the solid state using reducing agents, typically natural gas or hydrogen. The resulting product, often called sponge iron or its densified form, Hot Briquetted Iron (HBI), has gained increasing importance. This is not only due to its energy efficiency and ability to serve as a high-quality scrap alternative but also because of its crucial role as a key material in the transition to low-carbon steelmaking [22].

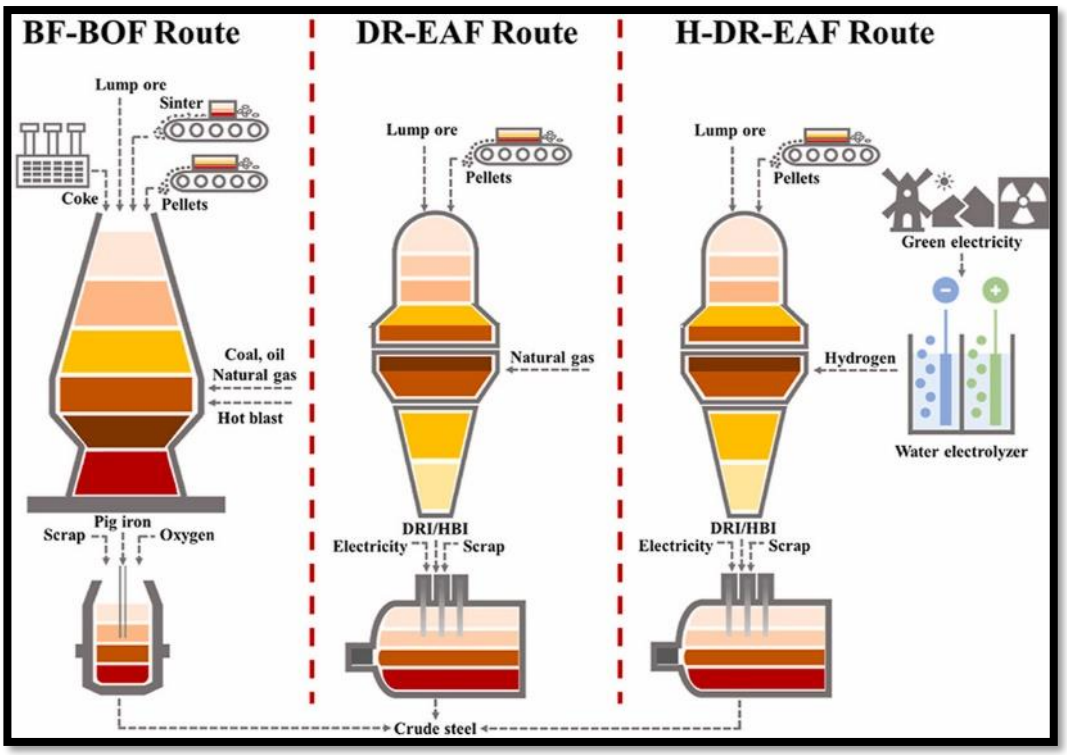


**Figure 2-5** Schematic comparison of conventional (BF-BOF), natural gas-based (DR-EAF), and hydrogen-based (H-DR-EAF) steelmaking routes.

#### 2.1.1.2 Ironmaking

In ore-based integrated production, ironmaking is primarily carried out in the blast furnace (BF). Iron oxide pellets or sinters are charged from the top of the furnace, along with coke and limestone. As this burden descends, it is gradually heated by ascending hot gases, which consist mainly of reducing agents such as carbon monoxide (CO) and hydrogen ($H_2$), along with reaction products including $CO_2$ and $H_2O$, as well as inert nitrogen ($N_2$). The reduction of iron oxides proceeds through a series of sequential transformations, in which hematite ($Fe_2O_3$) is first reduced to magnetite ($Fe_3O_4$), then to wüstite (FeO), and finally to metallic iron (Fe).

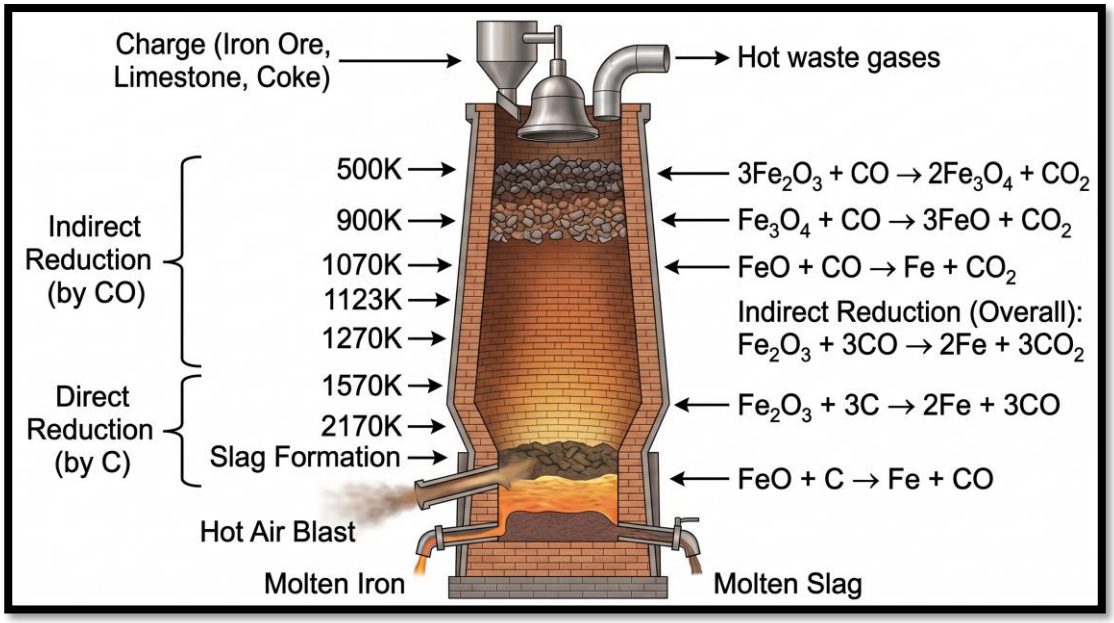


**Figure 2-6** Cross-sectional diagram of a blast furnace showing charge materials, slag formation, and the indirect/direct reduction zones. (Image generated by Gemini AI.)

The final stage of reduction occurs in the cohesive zone at high temperatures, typically exceeding 1600 °C, where wüstite (FeO) is reduced to molten metallic iron. Concurrently, impurities like silica (SiO2), alumina (Al2O3), magnesia (MgO), and sulfur (S), originating from the ore and coke, react with the flux (lime and dolomite) to form a molten slag. Historically, achieving enhanced desulfurization required increasing the slag volume to absorb more sulfur, a method that demanded excessive coke consumption. Today, however, desulfurization is routinely performed as a separate, highly efficient external step [13]. Modern methods involve the pneumatic injection of desulfurizing agents, such as calcium carbide (CaC2), into the hot metal, often while it is contained within a torpedo car. Nitrogen gas carries the agent through a refractory-lined lance submerged deep into the molten metal, significantly improving sulfur removal efficiency while minimizing the use of coke within the furnace.

In contrast to the integrated route, the Electric Arc Furnace (EAF) route operates primarily on solid feedstocks, using either recycled scrap metal or high-purity Direct Reduced Iron (DRI) [23]. Unlike the BF, which yields liquid hot metal, the EAF functions as a highly flexible furnace where the solid charge is rapidly melted using electric energy. While steel scrap remains the dominant feedstock due to its abundance, it often introduces undesirable tramp elements (e.g., copper and tin) that compromise steel quality. Consequently, high-purity DRI or HBI is utilized to balance the EAF charge, effectively diluting the concentrations of these tramp elements and ensuring the production of high-grade steel. This dual-feed strategy provides the EAF with the necessary operational flexibility and metallurgical control.

#### 2.1.1.3 Steelmaking

The conversion of hot metal into usable steel marks the defining stage of modern metallurgy. Molten iron derived from the blast furnace is saturated with impurities—primarily carbon, sulfur, and phosphorus—all of which must be meticulously removed or adjusted to achieve the desired quality and properties of the final product.

In integrated steel plants, this primary refining step is executed in the Basic Oxygen Furnace (BOF). Supersonic jets of pure oxygen are blown directly onto the molten bath, vigorously oxidizing the dissolved carbon and other impurities like silicon, manganese, and phosphorus. The resulting oxides combine with added burnt lime (CaO) to form a slag that absorbs and removes these unwanted elements. Since these oxidation reactions are highly exothermic, steel scrap is added to the charge (typically around 30%) to control the bath temperature and protect the furnace lining [13].

The raw steel tapped from the primary refining vessel is then transferred to the ladle for secondary refining, or ladle metallurgy, which is vital for chemical fine-tuning. This process begins with deoxidation to remove dissolved oxygen, which would

otherwise cause porosity during solidification. Elements with a strong oxygen affinity, such as aluminum or ferrosilicon, are added to form stable oxides that float out into the slag. Following this, precise alloying additions are made to achieve the target composition for specific steel grades, tailoring properties like strength and toughness.

Advanced ladle metallurgy encompasses processes such as desulfurization, degassing (removal of dissolved gases), and inclusion modification, often ensured through vigorous argon stirring to promote chemical uniformity. For example, specialized Interstitial-Free (IF) steels require controlled additions of titanium or niobium to neutralize interstitial elements, thereby enhancing formability. Technological innovations like the Injection Refining (IR) process further allow for precise chemical adjustment and flexible production of highly specialized grades.

Finally, after secondary refining, the molten steel is poured into the tundish, which acts as a buffer between the ladle and the mold, ensuring a steady, controlled flow. The steel is then solidified in the continuous caster into semi-finished forms such as slabs, blooms, or billets. Continuous casting has largely replaced older ingot casting methods, offering significant benefits including higher productivity, improved yield, and superior final product quality. This study will now focus on the subsequent downstream processing of these semi-finished products, specifically the hot and cold rolling operations applied to the continuously cast slabs.

#### 2.1.1.4 Hot Rolling

Hot rolling serves as the initial and primary deformation process for continuously cast steel slabs. This process drastically reduces slab thickness (e.g., from approximately 250 mm to a few millimeters in hot strip form) and is conducted at elevated temperatures, typically between 800 °C and 1200 °C. Operating within this range ensures the steel remains in the austenitic phase, guaranteeing high ductility and plastic deformability [13]. Although often considered an intermediate step

before cold rolling, hot rolling provides a significant share of the final product market directly. Hot-rolled products are fundamental materials widely utilized across major sectors, including construction, shipbuilding, and infrastructure, thus representing a substantial portion of global steel trade.

A necessary byproduct of this high-temperature process is the formation of oxide scale on the steel surface. This scale is multi-layered, consisting primarily of $Fe_2O_3$ (hematite), $Fe_3O_4$ (magnetite), and FeO (wüstite). The scale's thickness and specific composition are highly sensitive parameters that depend directly on the material's cooling rate and the final coiling temperature.

#### 2.1.1.5 Pickling

To prepare hot-rolled steel for subsequent processing, the oxide scale must first be removed via pickling, a process where the scale reacts chemically with strong acid solutions. Historically, sulfuric acid ($H_2SO_4$) was the primary agent, but hydrochloric acid (HCl) is now the preferred global standard due to its faster reaction kinetics and superior suitability for high-speed continuous strip lines [13]. Representative reactions are:

$$FeO+2HCl \rightarrow FeCl_2+H_2O$$

$$Fe_2O_3+6HCl \rightarrow 2FeCl_3+3H_2O$$

$$Fe_3O_4+8HCl \rightarrow FeCl_2+2FeCl_3+4H_2O$$

A typical continuous pickling line employs multiple tanks arranged in series, with the acid concentration strategically increasing in the downstream direction to maximize operational efficiency. Before immersion, scale breakers are often used to mechanically crack the brittle oxide layer, which significantly enhances acid penetration and pickling speed. The HCl solution dissolves the various iron oxide phases (wüstite, magnetite, and hematite) into ferrous and ferric chlorides. Crucially,

the process also requires the use of organic inhibitors to prevent the acid from corrosive attack on the underlying base metal, minimizing chemical loss.

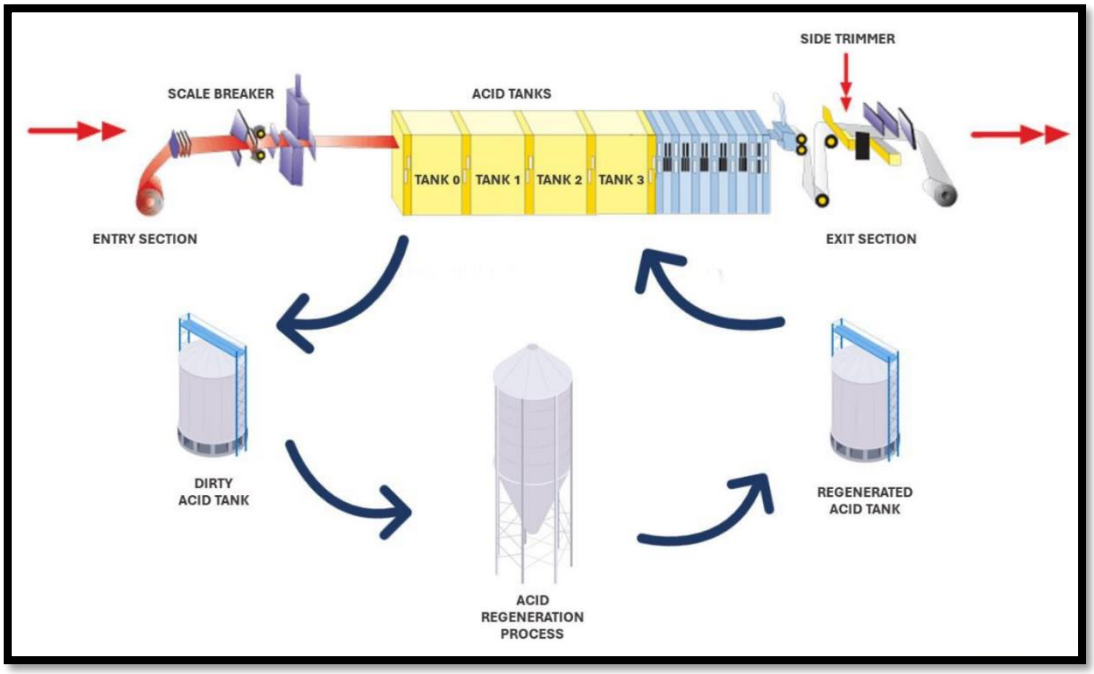


**Figure 2-7** Process Flow Diagram and Integrated Acid Regeneration Loop of the Borçelik Continuous Pickling Line (CPL).

Managing the resulting spent pickle liquor is critical for environmental sustainability. Modern facilities widely practice acid regeneration rather than disposal, as this reduces waste, minimizes safety hazards associated with transporting fresh acid, and maintains process continuity. The two dominant thermal regeneration methods, which boast acid recovery rates of over 99%, are spray roasting and fluidized-bed systems. Both rely on the thermo-pyrolysis of ferrous chloride to recover concentrated HCl gas and produce marketable iron oxide, thereby achieving a near-zero-waste process and enhancing overall system sustainability [25].

#### 2.1.1.6 Cold Rolling and Annealing

For applications demanding tighter dimensional tolerances and a superior surface finish, hot-rolled and pickled steel is subjected to cold rolling. This process is performed below the steel's recrystallization temperature, resulting in substantial thickness reduction, improved mechanical properties, and the production of smooth surfaces. While cold rolling significantly increases hardness and yield strength, it concurrently reduces the material's ductility due to work hardening.

To counteract the loss of ductility and relieve the internal stresses generated during deformation, subsequent annealing treatments are required. Techniques like batch annealing, open-coil annealing, or continuous annealing are applied to restore ductility and refine the microstructure. Specialized methods, such as intercritical annealing, may also be employed to optimize the balance between ferrite and austenite phases, allowing for precise tailoring of the final mechanical performance. In modern metallurgy, the combination of rolling and annealing operations is paramount, as these thermomechanical processes fundamentally dictate the resultant microstructure and, consequently, the mechanical properties essential for targeted steel design [26].

Because of the exceptional surface quality and precise dimensions achieved, cold-rolled steels are indispensable in sectors with strict aesthetic and performance requirements. These materials are critical, for instance, in the automotive industry for manufacturing visible body panels and in the production of household appliances.

#### 2.1.1.7 Finishing

The final stage of steel production encompasses finishing operations, which are essential for ensuring that products meet precise dimensional, mechanical, and surface requirements for the end-user. Mechanical finishing processes—including slitting, edge trimming, and shearing—are used to transform coils and sheets into the exact widths and sizes demanded by downstream manufacturers.

To impart corrosion resistance and extend service life, various surface finishing processes are widely employed. Hot-dip galvanizing represents the most common method, involving the immersion of steel into molten zinc. This creates a multi-layered barrier consisting of iron-zinc intermetallic phases (η, ζ, δ, Γ) that provide durable protection [27]. Alternative surface treatments include electro-galvanizing, various passivation and phosphate coatings, and the application of organic coatings (such as paints and polymers).

Ultimately, these stringent finishing steps guarantee that steel products not only satisfy structural and mechanical specifications but also achieve the aesthetic quality and durability required by modern, demanding applications.

### 2.1.2 Green Transition in the Steel Industry

The steel industry, a cornerstone of modern infrastructure, concurrently stands as one of the most significant contributors to global climate change. Conservative estimates hold the sector accountable for approximately 7% to 9% of global greenhouse gas (GHG) emissions (equating to roughly 2.6 billion tonnes of $CO_2$ annually), primarily due to its reliance on coal and fossil fuels in traditional production routes [14][23]. The widely adopted Blast Furnace-Basic Oxygen Furnace (BF-BOF) method is the chief source of these emissions, necessitating a comprehensive, systemic transformation to align the industry with international climate mitigation targets. This urgency has prompted major jurisdictions, notably the European Union (EU), to enact stringent policy frameworks to drive radical change.

The EU's decarbonization agenda, spearheaded by the European Green Deal (EGD), aims to achieve carbon neutrality by 2050, mobilizing sophisticated policy instruments to manage financial risk and market integrity. These instruments include the EU Emissions Trading System (EU-ETS), which establishes a carbon price, and the Carbon Border Adjustment Mechanism (CBAM), designed to mitigate carbon leakage (CL) by taxing carbon-intensive imports [28]. Mechanisms like Carbon

Contracts for Difference (CCfDs) are deployed to provide long-term financial assurance against fluctuating carbon prices, essential to de-risk high-capital investments in new technologies [28]. Despite these efforts, the literature reveals that the success of the transition is not solely technological but depends on managing the sociotechnical system (policy, finance, energy infrastructure) [23].

The core of the technological roadmap lies in achieving near-zero emissions by displacing fossil fuels. The most transformative pathway is the adoption of Hydrogen Direct Reduction ($H_2$-DR), which uses green hydrogen to generate only water vapor [22]. $H_2$-DR is recognized as the pathway with the highest potential for deep decarbonization, though its commercial viability hinges on the ability to supply green hydrogen at competitive costs, ideally below 2.5 USD/kg, necessitating massive investment in renewable energy, particularly offshore wind [29]. While $H_2$-DR represents the long-term solution, transitional technologies remain crucial for the mid-term. These include Carbon Capture and Storage/Utilization (CCS/CCU), which are considered feasible for retrofitting existing BF-BOF facilities [30]. Furthermore, CCU offers a dual environmental benefit by utilizing industrial solid waste, such as steelmaking slag, for $CO_2$ mineralization, effectively turning an environmental liability into a carbon sink [31].

However, the pursuit of deep decarbonization should not overshadow the cumulative potential of micro-scale improvements achievable through digitalization and process innovation. The integration of Artificial Intelligence (AI), advanced sensor technology, and predictive modeling is enabling incremental yet significant gains in energy efficiency, resource optimization, and waste reduction across all aspects of the steelmaking value chain. These micro-improvements, while less dramatic than $H_2$-DR, accumulate to create considerable cumulative change in a sector defined by thin margins and high volumes. This principle extends even to established operations like pickling.

The surface preparation phase, known as pickling, has historically relied on chemicals, primarily hydrochloric acid (HCl), to remove mill scale. While the

industry successfully mitigated the worst local environmental damage from spent acids decades ago through regeneration technologies like Spray Roasting [25] the process remains reliant on chemicals, energy, and water, carrying residual risks. The next definitive step in the green transition must, therefore, target the elimination of chemical dependence in such downstream operations. Integrating laser-based surface cleaning (laser descaling) into continuous pickling lines presents a compelling, ready-to-deploy process innovation. This technological shift would entirely bypass the need for acids and the associated regeneration equipment, offering a dry, chemical-free alternative. By adopting laser descaling, the steel industry can secure a further green transition in its finishing stages, providing a viable pathway for continuous pickling lines to evolve into a truly sustainable, zero-chemical-waste operation, thus demonstrating that innovation at the process level remains a vital component of the overarching decarbonization mandate.

In this thesis, the efficiency, energy consumption, and waste management aspects of laser-based descaling will be systematically evaluated as an alternative to conventional pickling.

### 2.1.3 Laser Descaling of Oxide Scales on Hot Rolled Steel Strip

The acronym "LASER" stands for "Light Amplification by Stimulated Emission of Radiation." Lasers are advanced optical devices that generate light beams characterized by specific wavelengths, high intensity, monochromaticity, and coherence. These unique properties make them indispensable across a broad spectrum of fields, ranging from industrial manufacturing to medical applications. The wavelength and intensity characteristics of the light produced by a laser depend primarily on the active gain medium (e.g., solid-state, gas, fiber) and the optical resonator structure used within the device. The energy, wavelength, and pulse characteristics of the resulting light directly determine the laser's capabilities on various materials. For instance, high-continuous-power $CO_2$ lasers are widely preferred for heavy industrial cutting processes, whereas Nd:YAG or fiber lasers,

which offer shorter wavelengths and higher peak powers, are more prominent in precision surface treatments and micro-machining.

While historically utilized primarily for fundamental manufacturing processes such as cutting, drilling, and welding, the application scope of laser technology is expanding rapidly due to advancing engineering capabilities and increased system precision. Today, lasers are employed for highly innovative and specific objectives, including laser cladding, laser surface hardening, and surface cleaning. At the forefront of these innovative applications is the laser descaling process. This technique fundamentally relies on the high energy carried by the laser beam being absorbed by the undesirable oxide layer on the surface, which is then removed from the base metal via an ablation (vaporization/spallation) mechanism. The interaction between the laser beam and the oxide layer is a complex thermophysical and thermomechanical process. Thanks to the precise control of optical and thermal penetration, the heat-affected zone (HAZ) is kept to a minimum, thereby preserving the integrity and mechanical properties of the underlying base metal [32].

Extensive research has been conducted in the literature regarding the laser-assisted cleaning of oxide layers on steel surfaces. These studies demonstrate that the efficiency of the process is strictly dependent on specific parameters such as laser power, wavelength, pulse energy, and scanning speed. In early studies, the use of lasers for cleaning the scale formed after hot-rolling on austenitic stainless steels was proposed as an environmentally friendly alternative to chemical pickling or abrasive blasting methods [33]. Subsequent research focused on the mechanical effect of the shock waves generated by the laser (stress wave-induced spallation). For example, Guo et al. [34] utilized Q-switched pulsed Nd:YAG lasers at 1070 nm and frequency-doubled 532 nm wavelengths to clean heavy oxide layers on SUS409 stainless steel. Their study demonstrated that a shorter wavelength, higher power density, and multiple-pulse irradiation improved surface cleaning, and that various combinations of pulse durations and scanning velocities did not lead to any loss in the underlying base metal. Similarly, Lim and Kim [35] employed a Q-switched Nd:YAG laser with a 1070 nm wavelength and a 6 ns (FWHM) pulse duration to remove scale from low-

carbon steels, inducing optical breakdown in an acid solution to create intense pressure waves that act as a non-contact scale breaker. In more recent studies, parameter optimization has been further detailed. Zhang et al. [36] used a ~100-ns high-repetition-frequency pulsed laser to clean the oxide layer on hot-rolled sheet surfaces. To prevent the formation of a secondary oxide layer caused by laser-induced heating, the researchers optimized the scanning speed, the spatial overlap between adjacent scans, and the laser power density. Aiming to clean the scale solely through thermomechanical destruction without reaching its melting point, Zhurba and his team [37] established a specific exposure regime using a continuous-wave (CW) fiber ytterbium laser with a maximum power of 2 kW. Therefore, to determine whether laser cleaning can be integrated as a sustainable and competitive alternative in flat steel manufacturing, it is essential to evaluate not only the surface quality and microstructural integrity but also the specific energy demands of the process under continuous operational conditions.

### 2.1.4 Scope and Objective of the Study

Addressing this critical void between laboratory-scale feasibility and industrial-scale applicability forms the core motivation of this research. Despite these extensive studies and detailed parameter optimizations (including varying wavelengths, nanosecond or microsecond pulse durations, and power densities reaching megawatt levels) in the literature, the laser cleaning process in hot-rolled flat steel production requires a renewed, comprehensive investigation. The primary reason is that, depending on the cooling rates in flat steel production processes, the thickness, morphology, and the proportions of the constituent phases (wüstite, magnetite, hematite) of the scale layer vary significantly. Since the absorption characteristics of the laser beam differ for each phase, a specific and dynamic regime must be established for flat steels. Furthermore, while the current literature focuses predominantly on the successful physical removal of the scale layer, there is a significant gap regarding the net energy calculation and green transition analysis at

an industrial scale. In other words, when comparing the energy consumed by the laser system with its overall yield, it remains unclear exactly how much profitability laser descaling will provide in an industrial continuous line. Therefore, this study will not only investigate the ablation efficiency and phase changes of the scale layer but will also provide a detailed discussion on the energy consumption, and overall operational profitability introduced by the utilization of laser technology.

# CHAPTER 3

## CHARACTERIZATION OF OXIDE LAYER ON HOT-ROLLED FLAT STEEL

To effectively develop and optimize a laser-based descaling process for hot-rolled flat steels, a profound understanding of the physical, chemical, and optical properties of the native oxide layer is a fundamental prerequisite. Extensive research in the literature has demonstrated that the formation, thickness, and microstructural evolution of this scale are highly sensitive to thermomechanical processing parameters and alloy chemistry. For instance, Chen and Yuen [38] established that the oxide scale developed on commercial hot-rolled strips exhibits a complex, multi-layered structure primarily consisting of hematite, magnetite, and wüstite. Their study highlighted that the final thickness and the relative proportions of these constituent phases are intricately linked to specific production variables, such as finishing temperatures, coiling temperatures, oxygen availability, and cooling rates [38].

Given this inherent variability driven by dynamic production conditions, relying solely on generalized literature data is insufficient for precise, industrial-scale process design. Therefore, a specific and systematic characterization of the oxide layers formed specifically on Borçelik's hot-rolled flat steels is critical to establishing a highly efficient and tailored laser interaction regime.

To achieve this, the current chapter follows a sequential analytical approach. First, the physical variations and morphology of the oxide layer are investigated to understand the scale thickness distribution across different samples. Subsequently, a detailed crystallographic phase analysis is conducted to determine the exact distribution of the constituent oxide phases within the scale. Finally, the identified oxide structures are subjected to UV-Vis-NIR spectroscopy to characterize their phase-dependent optical absorption properties. Revealing how these specific

structures interact with different wavelengths of light forms the critical scientific foundation for selecting the optimal laser source and defining the necessary parameters for successful ablation.

Accordingly, the subsequent sections of this chapter are structured to detail the material selection, microstructural variations, crystallographic makeup, and optical characterization of the oxide layer.

### 3.1.1 Material Selection and Sampling Strategy

The characterization of the native oxide layer is a fundamental prerequisite for evaluating the subsequent efficiency of laser-based removal. In this study, a robust experimental matrix was designed to encompass the wide range of metallurgical and thermal variations typically encountered in continuous flat steel processing lines. To protect proprietary industrial data and maintain confidentiality regarding commercial steel grades, a systematic coding nomenclature was adopted. Consequently, the ten selected hot-rolled steel coils were identified based on their country of origin and sequence, specifically designated as CHI-1 and CHI-2 (China), EGY-1 and EGY-2 (Egypt), FRA-1 and FRA-2 (France), KOR-1 and KOR-2 (South Korea), and TUR-1 and TUR-2 (Türkiye).

The selection of these specific coils was strategically aimed at observing the influence of several key parameters on scale morphology and its corresponding response to laser interaction. Primarily, the experimental set spans a broad spectrum of steel chemistries, including ultra-low carbon Interstitial Free (IF) steels, high-carbon grades, and specialized boron-alloyed varieties. This metallurgical diversity allowed for an in-depth investigation into how specific alloying elements—such as Chromium (Cr), Silicon (Si), and Manganese (Mn)—affect oxidation kinetics and the interfacial adhesion of the scale. Furthermore, the coils were categorized by their coiling temperatures, designated as "Moderate" and "High" levels. Since the thermodynamics of wüstite, magnetite, and hematite formation are strictly

temperature-dependent, this thermal history variable is critical for correlating available thermal energy with final scale thickness and phase distribution. Additionally, by incorporating materials sourced from five different countries, the study inherently accounts for the potential logistical impacts of long-distance maritime transportation and varying environmental storage conditions on the surface integrity and secondary oxidation of the flat steel products.

To ensure the integrity and reproducibility of the experimental results, a systematic preliminary verification and preparation procedure was executed. Prior to any microstructural analysis, the precise chemical composition of each coil was verified using Optical Emission Spectroscopy (OES). This crucial validation step confirmed that the elemental mass fractions aligned perfectly with the intended experimental matrix and provided the necessary data to calculate the carbon equivalents (CE) of the samples.

Following chemical validation, representative specimens were extracted and sectioned using precision cutting equipment under continuous liquid cooling. This specific extraction methodology was strictly adhered to in order to prevent any thermally induced alterations to the native oxide phases or mechanical spallation at the steel-oxide interface. The verified chemical profiles, origins, and key processing parameters for the coded experimental steel coils are summarized in Table 3.1. These carefully prepared specimens provide the foundational data for the subsequent high-resolution microstructural investigations detailed in the following sections.

**Table 3-1** Elemental composition (wt.%) and coiling temperature classifications of the experimental steel samples.

| Sample Code | Coiling Temp. | C (wt%) | Si (wt%) | Mn (wt%) | Cr (wt%) | Ni (wt%) | Cu (wt%) | Ceq |
|---|---|---|---|---|---|---|---|---|
| **CHI-1** | Moderate | 0.6620 | 0.2183 | 0.7105 | 0.1348 | 0.0070 | 0.0096 | 0.8470 |
| **CHI-2** | High | 0.0400 | 0.0112 | 0.2032 | 0.0400 | 0.0168 | 0.0209 | 0.0850 |
| **EGY-1** | Moderate | 0.0456 | 0.0270 | 0.1880 | 0.0120 | 0.0338 | 0.0496 | 0.0890 |
| **EGY-2** | High | 0.0404 | 0.0203 | 0.1810 | 0.0163 | 0.0290 | 0.0470 | 0.0820 |
| **FRA-1** | Moderate | 0.5935 | 0.1947 | 0.6835 | 0.2385 | 0.0066 | 0.0092 | 0.7900 |
| **FRA-2** | Moderate | 0.0023 | 0.0980 | 0.7100 | 0.0290 | 0.0120 | 0.0140 | 0.1450 |
| **KOR-1** | Moderate | 0.0026 | 0.0010 | 0.0630 | 0.0000 | 0.0000 | 0.0120 | 0.0140 |
| **KOR-2** | Moderate | 0.6650 | 0.1791 | 0.6893 | 0.2337 | 0.0143 | 0.0181 | 0.8610 |
| **TUR-1** | Moderate | 0.2904 | 0.3235 | 1.5500 | 0.0600 | 0.0800 | 0.2300 | 0.6380 |
| **TUR-2** | High | 0.0332 | 0.0224 | 0.1379 | 0.0567 | 0.0767 | 0.2015 | 0.0940 |

### 3.1.2 Microstructural Analysis and Oxide Layer Thickness Measurement

The accurate determination of the initial oxide layer thickness is a critical parameter for optimizing the subsequent laser cleaning process. To systematically evaluate the scale layer morphology and transverse thickness variations, cross-sectional specimens were extracted from three distinct regions across the width of each coil: the drive side (DS), the center (MID), and the working side (WS). These extracted specimens were hot-mounted in bakelite resin to preserve the delicate structural integrity of the steel-oxide interface. Subsequently, the mounted samples were subjected to standard metallographic preparation, involving progressive grinding and fine polishing, to achieve a scratch-free surface suitable for high-resolution imaging.

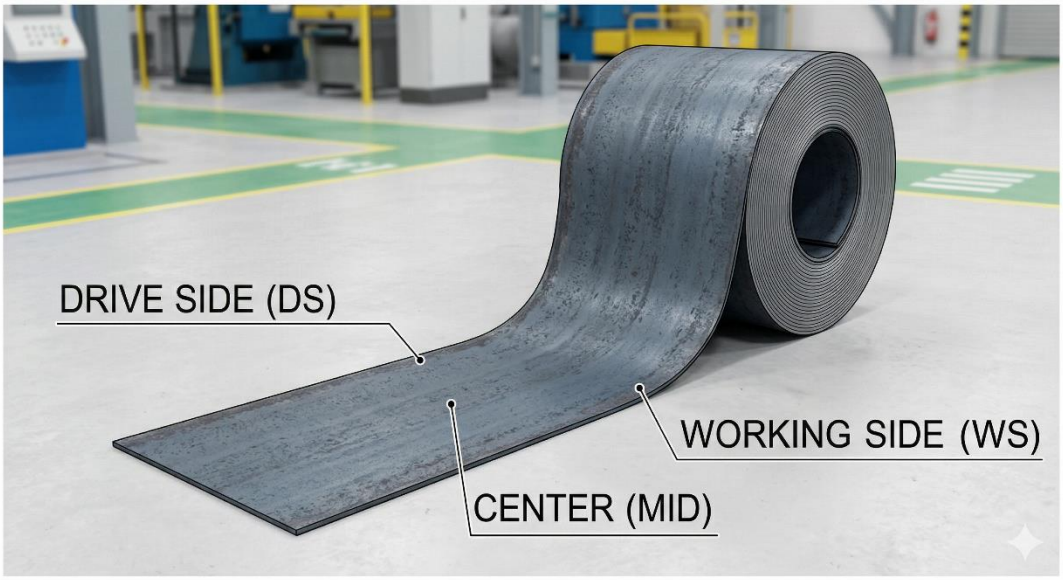


**Figure 3-1** A visualization of a flat-rolled steel strip, identifying key positional zones used for analysis. Leader lines clearly indicate the positions corresponding to the Drive Side (DS), Center (MID), and Working Side (WS) across the product width. (Image generated by Gemini AI.)

The cross-sectional microstructural examinations and precise thickness measurements were conducted using a Scanning Electron Microscope (SEM). To ensure the statistical reliability and representativeness of the data, a rigorous measurement protocol was implemented. For each specific region (DS, MID, and WS) of every coil, measurements were taken from six distinct, representative areas encompassing both the top and bottom surfaces. Two individual thickness readings were recorded per area, resulting in 12 data points per region and a total of 36 thickness measurements for each individual coil. To visually illustrate this precise measurement methodology, representative SEM micrographs detailing the cross-sectional scale thickness from the drive side (DS) of the CHI-1 sample are provided in Figure 3.2 as a baseline example. This standardized measurement approach, as depicted, was uniformly applied across all experimental specimens.

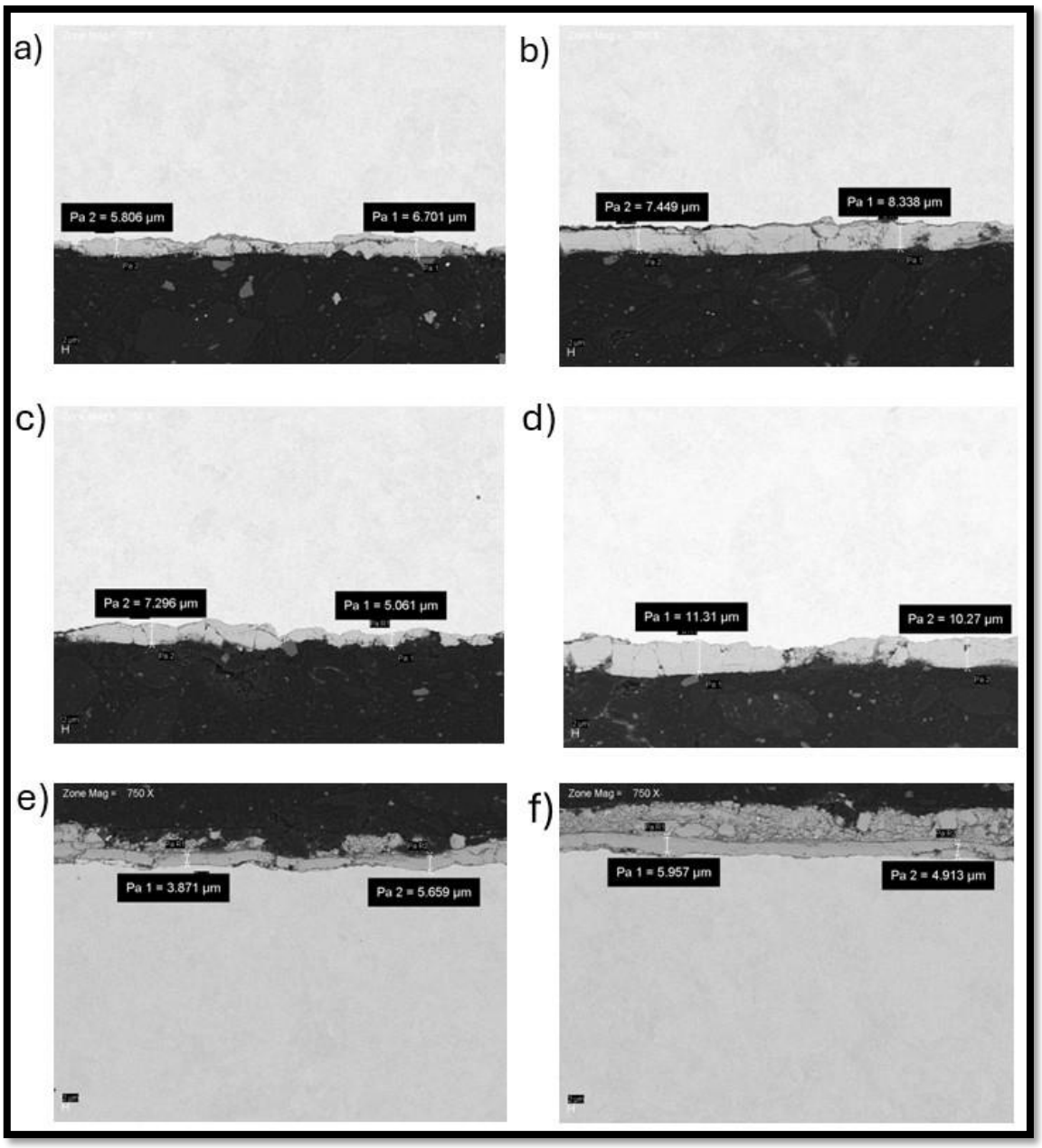


**Figure 3-2** Cross-sectional SEM micrographs detailing the oxide scale thickness from the drive side (DS) of the hot-rolled CHI-1 sample. The panels (a–f) illustrate the local variation in scale thickness across different measurement regions (750x magnification, scale bar = 2 µm).

To comprehensively understand the influence of varying chemical compositions and specific process parameters—such as coiling temperature—on oxide scale formation, the measurement methodology detailed for the CHI-1 sample in Figure 3-2 was systematically applied to all investigated specimens; the resulting statistical data, including mean thicknesses, standard deviations, and extremum values, are collectively presented in Table 3-2.

**Table 3-2** Statistical summary of oxide scale thicknesses (mean, standard deviation, minimum, and maximum in µm) measured across the strip width (drive side, middle, and work side) for the investigated hot-rolled steel samples.

| SAMPLE CODE | REGION | MEAN (µM) | STD. DEV. (µM) | MIN (µM) | MAX (µM) |
|---|---|---|---|---|---|
| **CHI-1** | DS | 6.49 | 1.98 | 3.87 | 11.31 |
| **CHI-1** | MID | 11.03 | 2.93 | 6.55 | 15.78 |
| **CHI-1** | WS | 6.68 | 1.73 | 4.47 | 10.27 |
| **CHI-2** | DS | 7.23 | 1.17 | 5.81 | 8.79 |
| **CHI-2** | MID | 8.49 | 0.71 | 7.30 | 9.68 |
| **CHI-2** | WS | 7.33 | 1.19 | 5.66 | 8.79 |
| **EGY-1** | DS | 12.11 | 4.42 | 6.10 | 18.17 |
| **EGY-1** | MID | 12.36 | 4.16 | 7.59 | 17.57 |
| **EGY-1** | WS | 12.63 | 4.06 | 6.70 | 18.16 |
| **EGY-2** | DS | 9.82 | 1.55 | 7.74 | 12.51 |
| **EGY-2** | MID | 8.93 | 1.14 | 7.59 | 11.31 |
| **EGY-2** | WS | 10.53 | 1.65 | 7.30 | 13.41 |
| **FRA-1** | DS | 8.63 | 1.50 | 6.40 | 11.46 |

| | | | | | |
|---|---|---|---|---|---|
| **FRA-1** | MID | 8.52 | 2.60 | 5.06 | 13.10 |
| **FRA-1** | WS | 8.18 | 1.65 | 4.91 | 10.72 |
| **FRA-2** | DS | 10.90 | 2.81 | 6.55 | 15.78 |
| **FRA-2** | MID | 12.14 | 2.05 | 8.63 | 15.22 |
| **FRA-2** | WS | 9.52 | 2.24 | 6.85 | 14.89 |
| **KOR-1** | DS | 10.88 | 2.30 | 7.74 | 15.78 |
| **KOR-1** | MID | 11.53 | 1.75 | 8.64 | 14.74 |
| **KOR-1** | WS | 9.55 | 1.95 | 6.70 | 13.25 |
| **KOR-2** | DS | 6.68 | 1.80 | 3.73 | 9.68 |
| **KOR-2** | MID | 11.27 | 2.20 | 7.89 | 15.33 |
| **KOR-2** | WS | 6.97 | 2.05 | 3.73 | 9.68 |
| **TUR-1** | DS | 5.78 | 1.35 | 3.88 | 8.49 |
| **TUR-1** | MID | 5.37 | 1.30 | 3.42 | 8.49 |
| **TUR-1** | WS | 4.90 | 0.85 | 3.58 | 6.56 |
| **TUR-2** | DS | 4.99 | 0.85 | 3.73 | 6.12 |
| **TUR-2** | MID | 9.66 | 1.50 | 7.59 | 12.06 |
| **TUR-2** | WS | 4.98 | 0.80 | 3.58 | 6.12 |

The statistical evaluation of the extensive measurement data reveals several critical morphological trends regarding the oxidation behavior of the coils. A predominant observation across almost all sampled coils is the pronounced transverse thickness gradient: the oxide layer at the center (MID) of the coils is consistently thicker than at the edges (DS and WS). This characteristic "crown" profile is directly attributable

to the thermal retention characteristics of the steel coil post-coiling. The edges of the coil are exposed to ambient conditions and cool at a significantly higher rate, whereas the core retains its thermal energy for a prolonged period. This extended time-temperature window at the center inherently promotes continuous oxidation kinetics, leading to substantial scale growth compared to the rapidly cooled edges.

Furthermore, a comparative analysis highlights distinct variations in scale thickness heavily influenced by the chemical composition of the steel, most notably the Silicon (Si) content. The data demonstrates a strong inverse correlation between the Si mass fraction and the resulting oxide layer thickness. For instance, the TUR-1 sample, which possesses the highest Si content (0.3235 wt.%) and high Manganese (Mn) content (1.55 wt.%) among the matrix, exhibits the thinnest and most uniform scale formation across all regions (averaging around 5 μm).

This empirical finding is strongly supported by the literature. Studies by Jia et al. [39] and Yang et al. [40] have extensively documented the retardation effect of Silicon on oxidation kinetics. Yang et al. [40] demonstrated that increasing Si content in hot-rolled steel strips leads to the formation of a Si-enriched inner oxide layer at the scale/substrate interface. This intermediate layer acts as a highly effective diffusion barrier, impeding the outward migration of iron cations and the inward penetration of oxygen atoms, thereby significantly decreasing both the oxidation rate and the overall scale thickness. Consequently, the notably thin scale observed in the TUR-1 sample is a direct manifestation of this Si-induced barrier effect.

Conversely, coils originating from Egypt (EGY-1 and EGY-2), which feature considerably lower Si contents, exhibit the thickest oxide layers among the experimental group, frequently exceeding 12-15 μm. Despite these chemistry- and origin-based variations, the overall dataset indicates that the oxide layer thickness for the evaluated hot-rolled flat steels predominantly concentrates within a targeted operational range of 5 μm to 12 μm.

Based on these morphological findings and the consistently observed transverse thickness gradient, a critical methodological decision was established for the

subsequent laser ablation experiments. Since the center (MID) region consistently exhibits the maximum oxide layer thickness across all sampled coils, it inherently represents the "worst-case scenario" for the oxide removal process. Consequently, it was decided that all experimental investigations regarding laser parameter optimization will be exclusively conducted on the MID specimens. The rationale behind this approach is robust: if the determined laser parameters (power density, scanning speed) possess sufficient energy to completely ablate the thickest scale layer without inducing thermal damage to the underlying steel substrate, they will inherently be effective for the thinner and less stubborn oxide layers present at the coil edges. This strategic selection ensures the development of a reliable and universally applicable operational window for continuous industrial processing lines.

While establishing this macroscopic "worst-case" thickness model is vital for estimating the baseline energy required for laser ablation, thickness alone does not dictate the removal efficiency. The thermo-mechanical interaction between the laser beam and the oxide layer is equally governed by the specific crystallographic nature and the interfacial adhesion of the scale. Identifying the precise phase fractions—specifically the distinct proportions of wüstite, magnetite, and hematite—is essential, as each phase exhibits significantly different light absorption coefficients and ablation thresholds. Consequently, to gain a deeper microstructural understanding beyond mere morphological thickness, advanced crystallographic investigations utilizing Electron Backscatter Diffraction (EBSD) were subsequently performed on these selected worst-case MID samples. The detailed findings regarding these phase formations and their specific distributions within the scale layer are discussed in the following section.

## 3.2 Crystallographic Phase Analysis via Electron Backscatter Diffraction

While cross-sectional thickness measurements provide a macroscopic understanding of the scale morphology, the phase composition of the oxide layer plays a decisive role in determining the energy absorption and subsequent ablation efficiency during

laser cleaning. To investigate the crystallographic characteristics of the scale, four representative samples were strategically selected from the experimental matrix: TUR-1, TUR-2, FRA-1, and KOR-1. Each selection serves as a specific metallurgical or process benchmark; TUR-1 represents the standard commercial production baseline, TUR-2 was chosen to observe the influence of high coiling temperatures on phase transformation, FRA-1 facilitates the evaluation of high-carbon content on oxidation kinetics, and KOR-1 provides a perspective on the oxidation behavior of low-carbon steel grades.

The high-resolution EBSD analyses were conducted at the Diler Demir Çelik Recep Sami Yazıcı Product Development Center. In addition to the standard metallographic preparation previously described, these specimens underwent an advanced final polishing stage to meet the stringent surface requirements of EBSD analysis. A fumed silica suspension with a particle size of 0.25 μm was utilized to achieve an ultra-fine finish, effectively removing any residual surface deformation layers and ensuring high-quality diffraction patterns. The crystallographic data were collected from multiple representative regions of each specimen to ensure a statistically sound distribution of the constituent phases.

Following metallographic preparation, the specimens were subjected to EBSD analysis to meticulously identify and quantify the constituent oxide phases. The spatial distribution of these phases is visually presented first in the representative EBSD phase maps provided in Figure 3-3.

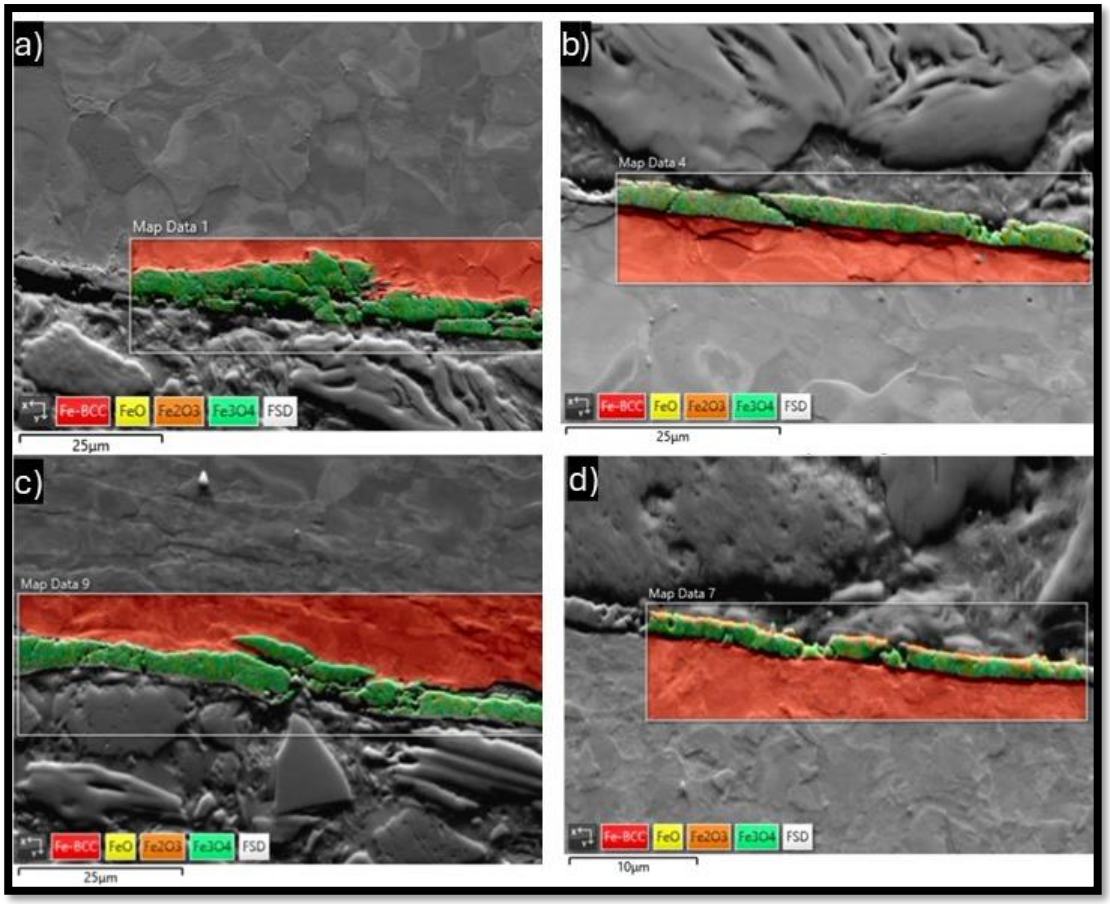


**Figure 3-3** Cross-sectional EBSD phase maps revealing the oxide scale constitution and spatial phase distribution of the representative samples: (a) TUR-1 (standard baseline), (b) TUR-2 (high coiling temperature), (c) FRA-1 (high-carbon grade), and (d) KOR-1 (low-carbon grade).

While the SEM-based images presented previously provide a clear overview of the scale's cross-sectional morphology, they do not possess the necessary crystallographic contrast to distinctly differentiate between the individual oxide phases. To accurately resolve and visualize the spatial distribution of hematite, magnetite, and wüstite, high-resolution EBSD phase maps were subsequently generated. These detailed phase distributions, which provide a much deeper insight into the scale's constitution, are presented on the Figure 3-4.

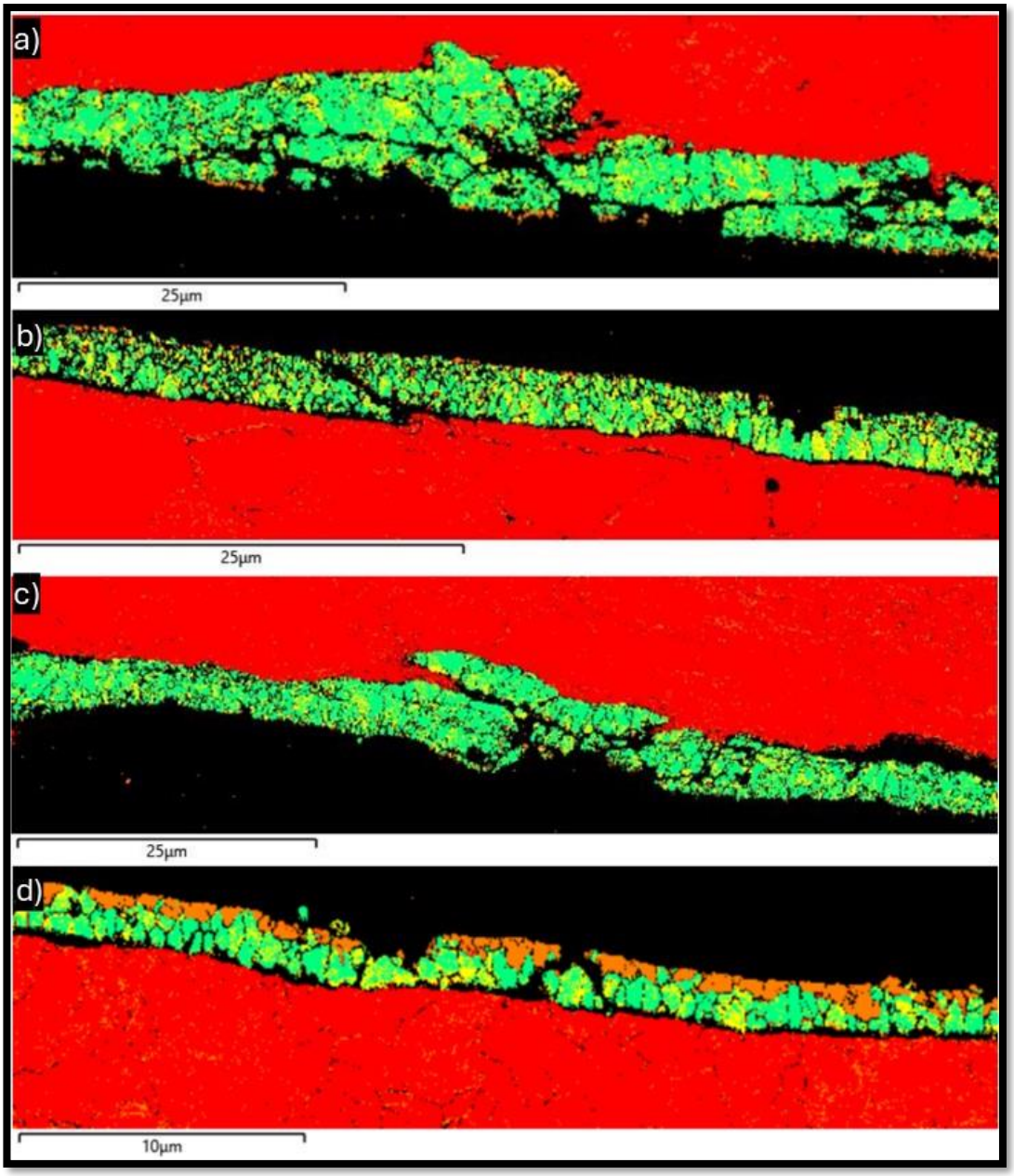


**Figure 3-4** High-resolution EBSD phase maps providing a detailed spatial distribution of the identified oxide phases (Hematite, Magnetite, and Wüstite) for the representative specimens: (a) TUR-1, (b) TUR-2, (c) FRA-1, and (d) KOR-1.

A qualitative assessment of these phase maps reveals a distinct stratified structure. Hematite formation is almost entirely restricted to the outermost surface of the scale,

and its presence is visually striking in the KOR-1 specimen. Beneath this superficial layer, magnetite constitutes the dominant bulk phase across all samples, while wüstite acts as a secondary phase located deeper towards the steel-scale interface. The precise quantitative phase fractions derived from the EBSD analysis are summarized in Table 3-3.

**Table 3-3** Quantitative phase fractions of the oxide layers derived from EBSD analysis.

| Sample Code | Hematite ($Fe_2O_3$) (%) | Wüstite (FeO) (%) | Magnetite ($Fe_3O_4$) (%) |
|---|---|---|---|
| **TUR-1** | 4.61 | 22.64 | 72.79 |
| **TUR-2** | 6.69 | 38.98 | 54.33 |
| **FRA-1** | 24.85 | 26.85 | 45.27 |
| **KOR-1** | 6.35 | 29.88 | 66.80 |

As detailed in Table 3-3, magnetite remains the predominant oxide, forming the majority of the scale volume. However, a critical variation is observed in the hematite concentration, specifically in the KOR-1 specimen. While most samples exhibited a limited hematite presence of approximately 4–6%, KOR-1 showed a significantly higher fraction of 24.85%, heavily concentrated at the extreme outer surface. This variation is intrinsically linked to the steel's carbon chemistry; since KOR-1 is a low-carbon grade, there is minimal outward diffusion and evolution of carbon monoxide/dioxide ($CO/CO_2$) gases from the steel substrate during high-temperature oxidation. The absence of these locally reducing outward gas flows allows the oxygen partial pressure at the extreme outer surface to remain high, thereby promoting the extensive further oxidation of magnetite into hematite [41].

Furthermore, the presence of wüstite, although varying between 22.64% and 38.98%, is primarily observed in the inner regions of the scale. This distribution is a

direct consequence of the continuous cooling transformation post-coiling; as the temperature drops below 570°C, the unstable wüstite phase typically undergoes a eutectoid decomposition into magnetite and proeutectoid ferrite, a process that significantly dictates the final phase ratios observed in the EBSD data [42].

This surface-heavy distribution of hematite, combined with the massive prevalence of bulk magnetite beneath it, creates a critical optical dynamic for the laser descaling process. The incident laser beam will definitively interact with the surface hematite layer first, followed by the underlying magnetite. Since wüstite is located much deeper within the scale matrix, its direct optical interaction during the initial laser pulse is less critical. Consequently, to optimize the ablation mechanism, it is essential to select a specific laser wavelength based on the distinct absorption and transmission characteristics of hematite and magnetite. To accurately determine the optimal wavelength that interacts most efficiently with these two primary phases, UV-Vis-NIR spectroscopy tests were subsequently performed..

## 3.3 Optical Property Characterization and Laser Source Selection

As established by the EBSD analysis in Section 3.2, the oxide scale on the investigated hot-rolled steel coils is predominantly composed of magnetite, with varying minor fractions of hematite and interfacial wüstite. Since laser-based oxide removal is fundamentally a photothermal ablation process, the efficiency of this operation is directly governed by the optical absorption characteristics of these specific crystallographic phases. To accurately determine the interaction behavior between the incident laser beam and the oxide layer across the electromagnetic spectrum, UV-Vis-NIR (Ultraviolet-Visible-Near Infrared) spectroscopy was conducted.

The spectroscopic measurements were carried out at the Bartın University Central Research Laboratory. The primary objective of this spectral analysis was to quantify the absorbance of the dominant magnetite and hematite phases to identify the most

thermodynamically efficient laser wavelength. The comparative absorption spectra for both hematite and magnetite, recorded as a function of wavelength, are illustrated in Figure 3.4.

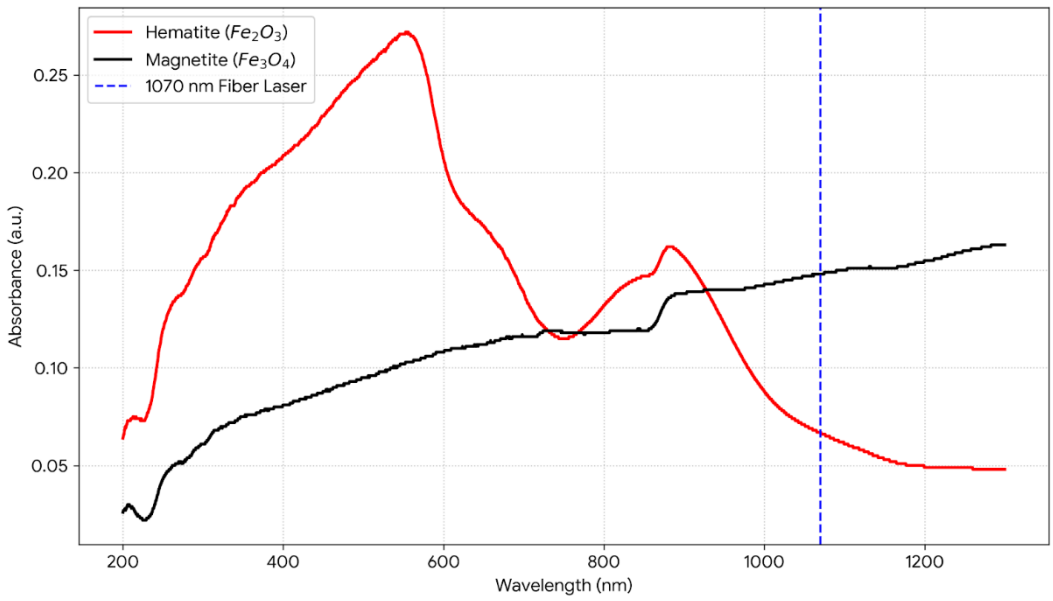


**Figure 3-5** UV-Vis-NIR Absorption Spectra of Oxide Phases

The spectroscopic data reveals critical insights into the phase-specific optical behaviors that directly dictate the ablation mechanism. While the absorption dynamics fluctuate significantly in the ultraviolet and visible regions, the Near-Infrared (NIR) spectrum demonstrates a highly stable and effective absorption profile, particularly for magnetite. Magnetite, functioning as an inverse spinel with active intervalence charge transfer between $Fe^{2+}$ and $Fe^{3+}$ octahedral sites, exhibits a near-metallic optical conductivity. Consequently, it strongly absorbs incident energy across the broad NIR spectrum. This is of paramount importance because magnetite constitutes the bulk volumeof the scale layer in all investigated specimens.

Conversely, hematite , which possesses a bandgap of approximately 2.1 eV, exhibits strong absorption in the UV and visible ranges but becomes relatively transmissive (less absorbing) in the NIR region. This optical disparity is highly advantageous for

the cleaning process, particularly for low-carbon grades like KOR-1 that feature a hematite-rich outer surface. When a NIR laser beam irradiates the surface, it partially penetrates the transmissive outermost hematite layer and intensely couples with the underlying bulk magnetite. The rapid, localized subsurface heating of the magnetite layer induces massive thermal expansion and phase transformation, which subsequently results in explosive thermomechanical spallation. This mechanism effectively blasts away the entire scale layer from the inside out, including the outer hematite, ensuring complete surface cleaning without requiring the surface phase to directly absorb the optical energy.

Based on these UV-Vis-NIR absorption results and the compositional dominance of magnetite, the optimal wavelength for the experimental oxide removal process was unequivocally determined to be in the NIR region, specifically at 1070 nm. At this wavelength, the magnetite phase maintains a strong and consistent optical absorption capacity, ensuring rapid photothermal conversion.Furthermore, the selection of a 1070 nm continuous-wave/pulsed fiber laser is highly strategic from an industrial and green transition perspective. Ytterbium-doped fiber lasers operating at this wavelength are commercially mature, widely accessible, and offer an exceptionally high wall-plug efficiency (often exceeding 30%). If a wavelength with diminished absorption for magnetite were chosen, the incident optical energy would be inefficiently scattered or reflected, significantly lowering the overall ablation efficiency and requiring excessive energy input that could thermally damage the underlying steel substrate. Therefore, utilizing the 1070 nm fiber laser ensures maximum energy coupling with the "worst-case" thick magnetite layers while providing the most viable, scalable, and energy-efficient alternative to traditional acid pickling in continuous flat steel processing lines.

The subsequent chapters will detail the experimental setup, parameter optimization (power, and scanning speed), and the evaluation of the cleaned surfaces utilizing this strategically selected 1070 nm fiber laser source.

# CHAPTER 4

## EXPERIMENTAL INVESTIGATION OF LASER-BASED OXIDE REMOVAL

The experimental oxide removal trials were conducted utilizing an industrial-grade, automated laser processing system located at the ERMAKSAN research and development facility. The system is equipped with a high-power fiber laser source operating at a fixed fundamental wavelength of 1070 nm. This specific wavelength was deliberately selected as it aligns perfectly with the high optical absorption characteristics of the magnetite-rich scale established in the previous chapter.

It is important to note that due to proprietary intellectual property (IP) policies and commercial confidentiality agreements with the facility, the specific architectural details, internal optical train configurations, and proprietary software interfaces of the laser machinery are intentionally omitted from this dissertation.

To ensure high precision, reproducibility, and uniform energy distribution, the laser optical head is integrated into a computer-controlled, 3-axis Cartesian gantry system. This automated mechanical framework operates on a principle similar to advanced CNC machinery, allowing the laser head to move freely and accurately across the X, Y, and Z axes. This automation is a critical component of the experimental design; it guarantees that the laser beam maintains a strictly uniform scanning speed across predefined target areas on the steel surface, completely eliminating the interaction inconsistencies and localized overheating risks associated with manual or handheld operation.

Based on the morphological baseline and the "worst-case scenario" methodology established during the characterization phase, the center (MID) specimens of the TUR-1 commercial grade steel were selected as the primary substrate for these parametric optimization trials. Prior to laser exposure, the specimens were securely

mounted on the experimental working bed, and the focal distance was precisely calibrated and kept constant to ensure a consistent spot size. The visual representation of the experimental apparatus, the automated gantry configuration, and the designated target zones on the representative TUR-1 specimens are provided in Figure 4.1 and Figure 4.2.

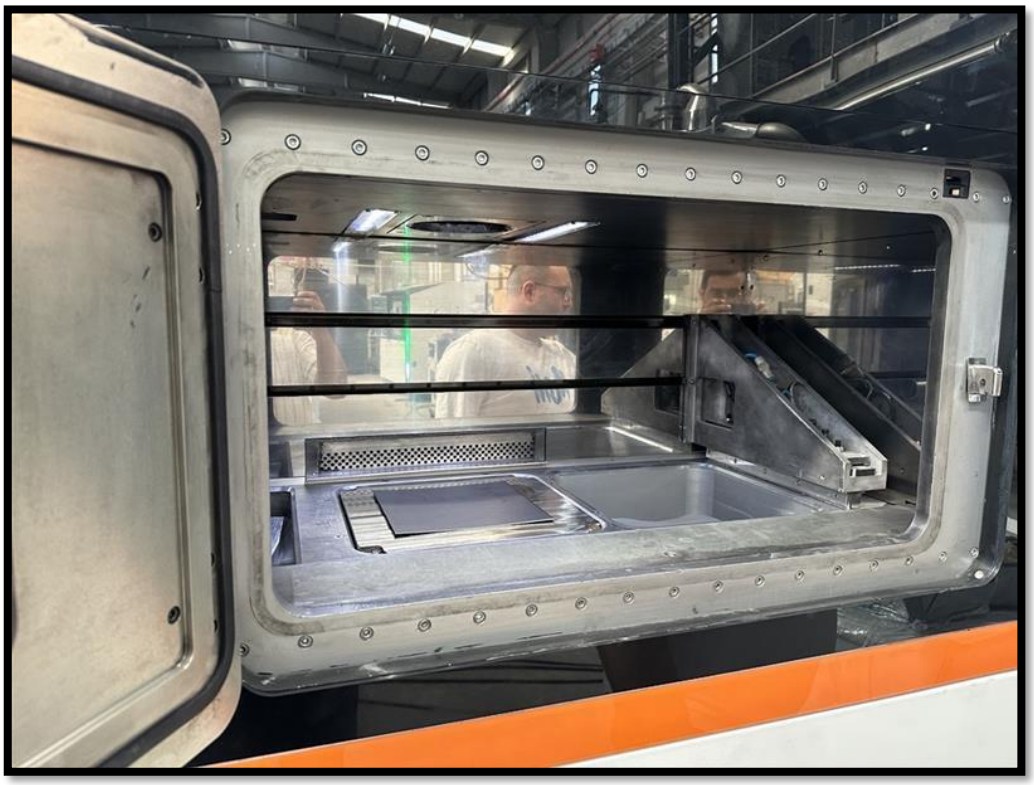

**Figure 4-1** A photograph of the setup used for the experiments

**Figure 4-2** Sample of a laser-exposed specimen

The core logic of the experimental design is predicated on finding the precise thermal balance for effective ablation. To systematically determine the optimal cleaning threshold, the experimental matrix was designed to test varying combinations of primary process parameters, predominantly Laser Power (P) and Area Scanning Speed ($v_{area}$). By modulating these variables, the study aims to identify the specific operational window that provides sufficient photothermal energy to completely vaporize the 5-12 μm thick oxide layer, while remaining safely below the melting or heat-affected zone (HAZ) threshold of the underlying steel substrate.

## 4.1 Continuous-Wave (CW) Laser Cleaning Experiments

The initial phase of the experimental investigation utilized the laser system in Continuous-Wave (CW) emission mode. The primary objective was to establish a fundamental baseline for oxide removal efficiency and to determine if continuous optical power could effectively ablate the scale layer. To ensure consistency and enable a direct thermodynamic comparison with subsequent trials, the experimental matrix utilized four distinct power levels (100 W, 200 W, 300 W, and 500 W) across a broad spectrum of area scanning speeds, systematically decreasing from 500 $mm^2/s$ down to 50 $mm^2/s$.

Visual inspections and detailed Scanning Electron Microscopy (SEM) investigations of the CW-processed specimens revealed a consistent failure to achieve a cleaned, scale-free surface across all parametric combinations. More importantly, cross-sectional SEM analysis highlighted a highly erratic morphological response. Depending on the specific power and speed combination, the oxide layer marginally decreased in certain specimens, while in others, the thickness of the oxide scale paradoxically and significantly increased compared to the un-irradiated baseline.

This erratic behavior—particularly the unexpected thickening of the scale—is directly attributed to the extreme thermal accumulation inherent in continuous emission kinetics. In CW mode, the laser delivers an uninterrupted stream of photothermal energy. Without the thermal relaxation time provided by pulsed systems, the continuous heat input deeply penetrated the material, elevating the temperature of the underlying steel substrate well above its critical oxidation threshold.

Consequently, the process shifted from optical ablation to high-temperature thermochemical oxidation. Metallic iron (Fe) atoms from the intensely heated steel substrate rapidly diffused outwards and reacted with atmospheric oxygen, forming a thick, secondary oxide layer (re-oxidation). Essentially, the continuous laser energy

acted as a heat source that fostered rapid new oxide growth rather than cleanly removing the existing scale [43].

These empirical findings conclusively demonstrate that Continuous-Wave emission is thermodynamically unsuitable for industrial descaling applications, as it inherently triggers secondary oxidation and thermal degradation. This critical limitation strictly necessitated the transition to Pulsed-Wave (PW) emission, where ultra-short pulses can provide the precise thermal confinement required for effective material removal without damaging the underlying steel.

## 4.2 Pulsed Wave Laser Cleaning Experiments

To overcome the inherent thermal limitations of the Continuous-Wave (CW) mode—specifically the critical issues of secondary re-oxidation and substrate thinning—the experimental focus was transitioned to Pulsed-Wave (PW) emission. The fundamental motivation for this shift is the phenomenon of thermal confinement. By delivering laser energy in ultra-short pulses (350 ns) with high peak power, the oxide scale rapidly reaches its ablation threshold and vaporizes almost instantaneously. This rapid photothermal conversion ensures that the cleaning process is completed before significant heat can conduct into the underlying metal substrate, thereby preserving the metallurgical integrity of the steel.

During the PW parametric trials, the morphological evolution of the surface was closely monitored. Based on detailed Scanning Electron Microscopy (SEM) observations of varying energy inputs, the laser-induced ablation mechanism of the oxide scale was systematically classified into five distinct evolutionary stages:

- Stage 0 (Initial State): The native, un-irradiated surface covered entirely by the multi-layered oxide layer.
- Stage 1 (Crack Initiation and Local Spallation): At insufficient energy levels, the laser induces thermal stress, causing micro-cracking and the localized flaking of the outermost scale layer. The bulk oxide remains intact.

- Stage 2 (Partial Ablation): As energy density increases, significant portions of the scale are vaporized; however, the cleaning is heterogeneous, leaving distinct un-ablated "islands" of scale across the surface.
- Stage 3 (Residual Traces): The surface is predominantly metallic iron, but isolated, stubborn microscopic residues of interfacial oxides remain.
- Stage 4 (Complete Descaling): The optimal operational threshold. The oxide layer is entirely vaporized, completely exposing the clean, bare metallic iron substrate without inducing thermal melting.

The visual representation of these sequential ablation phases is provided in Figure 4.3, which details the cross-sectional morphological changes from the initial un-irradiated state to a fully cleaned surface.

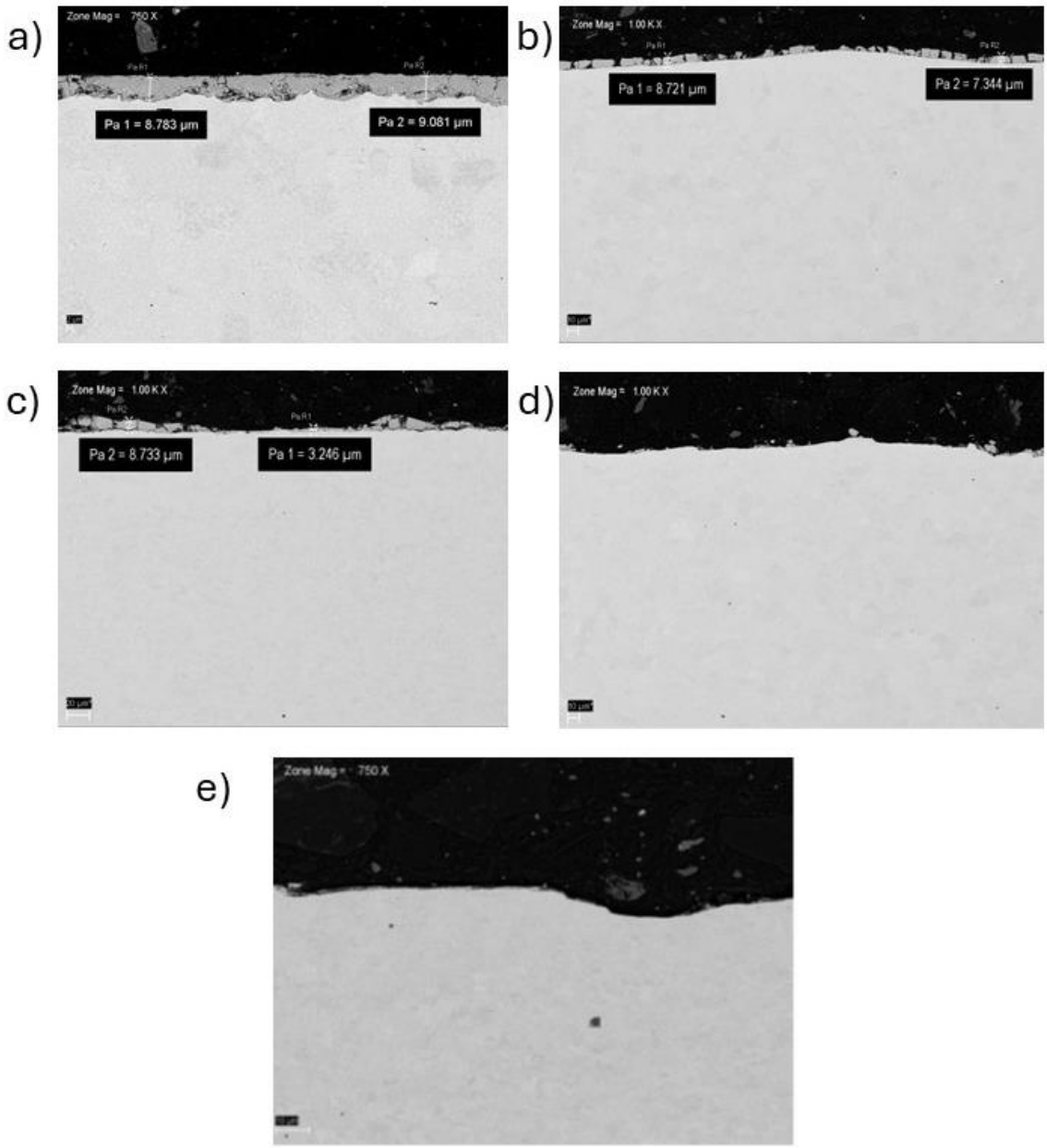


**Figure 4-3** Cross-sectional SEM micrographs illustrating the morphological evolution of the oxide scale across the defined ablation stages under pulsed-wave (PW) laser irradiation. The panels sequentially demonstrate: (a) Stage 0, the initial intact mill scale; (b) Stage 1, crack initiation and localized superficial spallation; (c) Stage 2, partial ablation leaving un-ablated oxide islands; (d) Stage 3, a predominantly clean surface with trace interfacial residues; and (e) Stage 4, complete and uniform descaling exposing the bare metallic iron substrate without thermal damage.

The PW experimental matrix was conducted to systematically map these stages and target the Stage 4 threshold. To establish a rigorous scientific baseline for comparison with the CW results, a comprehensive range of area scanning speeds from 500 $mm^2/s$ down to 50 $mm^2/s$ was evaluated across four distinct average power levels: 100 W, 200 W, 300 W, and 500 W. The processed specimens were characterized using SEM for morphological analysis and Energy-Dispersive X-ray Spectroscopy (EDS) to verify the total removal of oxygen.

The comprehensive results of this parametric sweep are systematically mapped in Table 4.1. This matrix visualizes the morphological evolution of the scale across forty distinct operational combinations of laser power and scanning speed.

**Table 4-1** Morphological evolution of the oxide scale (ablation stages) across the Pulsed-Wave (PW) experimental parameter matrix

| *Area Scanning Speed ($mm^2/s$)* | *100 W* | *200 W* | *300 W* | *500 W* |
|---|---|---|---|---|
| *50* | Stage 4 | Stage 4 | Stage 4 | Stage 4 |
| *100* | Stage 3 | Stage 4 | Stage 4 | Stage 4 |
| *150* | Stage 3 | Stage 3 | Stage 4 | Stage 4 |
| *200* | Stage 3 | Stage 3 | Stage 4 | Stage 4 |
| *250* | Stage 2 | Stage 3 | Stage 3 | Stage 4 |
| *300* | Stage 2 | Stage 2 | Stage 3 | Stage 4 |
| *350* | Stage 2 | Stage 2 | Stage 3 | Stage 4 |
| *400* | Stage 2 | Stage 2 | Stage 2 | Stage 4 |
| *450* | Stage 1 | Stage 1 | Stage 2 | Stage 4 |
| *500* | Stage 1 | Stage 1 | Stage 1 | Stage 2 |

As clearly demonstrated in the matrix, there is a pronounced diagonal shift in the ablation threshold. At the lowest power setting (100 W), the system lacks the rapid thermal intensity required for continuous vaporization at high speeds, restricting the Stage 4 (Complete Descaling) window strictly to 50 $mm^2/s$. Any slight increase in speed at this power level immediately drops the cleaning efficiency into Stage 3 or Stage 2. Conversely, as the laser power scales up to 500 W, the operational window expands dramatically. The high peak power delivered at 500 W provides sufficient instantaneous photothermal energy to completely overcome the ablation threshold of

the magnetite-rich scale, even at highly accelerated kinematics. Consequently, the Stage 4 threshold extends all the way up to 450 $mm^2/s$.

Extracting the successful Stage 4 parameters from this matrix highlights a critical relationship between laser power and industrial efficiency. While a clean surface was achieved at all power levels within their specific velocity windows, the energy efficiency improved dramatically at higher powers. As summarized in Table 4.2, the specific energy required to clean a unit area dropped significantly as the power increased.

**Table 4-2** Successful PW Cleaning Parameters (Stage 4) and Energy Efficiency Metrics.

| *Laser Power (W)* | *Successful Area Speed ($mm^2/s$)* | *Cleaning Rate ($m^2/h$)* | *Specific Energy ($J/mm^2$)* |
|---|---|---|---|
| *100* | 50 | 0.18 | **2.00** |
| *200* | 100 | 0.36 | **2.00** |
| *300* | 200 | 0.72 | **1.50** |
| *500* | 450 | 1.62 | **1.11** |

The specific energy required for complete ablation drops significantly from 2.00 $J/mm^2$ at 100 W to only 1.11 $J/mm^2$ at 500 W. This data conclusively demonstrates a critical thermodynamic trend: as the laser power scales up, the specific photothermal energy required to achieve complete descaling decreases. Consequently, high-power pulsed lasers not only enable significantly faster processing speeds—reaching cleaning rates up to 1.62 $m^2/h$—but also operate with maximized energy efficiency.

# CHAPTER 5

# INDUSTRIAL FEASIBILITY AND PERFORMANCE ANALYSIS

As the global steel industry pivots toward the "Green Transition" and decarbonization, traditional chemical-intensive processes such as acid pickling are under increasing scrutiny. Laser-based descaling emerges as a highly promising, dry, and sustainable alternative that eliminates chemical waste while offering a direct path to reducing the carbon footprint of flat steel production. This chapter evaluates the industrial feasibility of integrating high-power pulsed fiber lasers into existing production lines by comparing their energy dynamics, operational advantages, and current limitations against conventional Continuous Pickling Lines (CPL).

## 5.1 Operational Comparison: Pickling vs. Laser Cleaning

Conventional acid pickling relies on the chemical dissolution of iron oxides in heated hydrochloric acid baths. This mature technology, however, entails significant environmental liabilities and indirect energy costs. A critical burden for modern CPL facilities is the dependency on Acid Regeneration Plants (ARP), which utilize natural gas combustion to recover spent acid, thereby contributing substantially to a facility's direct $CO_2$ emissions.

A growing challenge in contemporary steelmaking is the increasing reliance on Electric Arc Furnace (EAF) production to utilize scrap steel. This transition introduces higher concentrations of trace elements, particularly Copper (Cu), into the steel substrate. During the pickling process, copper ions accumulate in the acid bath and tend to redeposit onto the steel surface—a phenomenon known as "copper plating." This unwanted deposition severely impairs the adhesion and quality of subsequent coatings. While conventional lines may require additional electrochemical treatments or electrolysis to manage copper levels, adding

significant operational complexity and cost [44], laser cleaning inherently bypasses this issue. As a non-chemical and purely physical process, there is no liquid medium for ion accumulation, ensuring a consistently clean surface regardless of the scrap-to-ore ratio.

## 5.2 Energy Comparison Methodology and Decarbonization

To conduct a rigorous feasibility analysis, the energy profiles of both the conventional Continuous Pickling Line (CPL) and the proposed laser cleaning system must be normalized into a single unit of measurement. For this purpose, the operational baseline for the conventional process was established using the actual 2025 production data from the Borçelik CPL. While laser systems operate purely on electrical energy, conventional lines utilize a hybrid energy mix, predominantly relying on natural gas for acid regeneration.

The utility consumption per metric ton of processed steel is summarized in Table 5.1. A standard CPL requires a direct electrical input of 8.0 kWh alongside a significant natural gas demand of 2.1 $Sm^3$ per ton. To achieve energy parity, the natural gas consumption was converted into its electrical equivalent using the BOTAŞ lower heating value (LHV) of 10.64 kWh/$Sm^3$ [46]. Consequently, the 2.1 $Sm^3$ of gas equates to 22.34 kWh, bringing the total energy footprint of a conventional CPL to 30.34 kWh/ton.

The energy consumption for the laser system was calculated based on the optimized experimental specific energy (1.11 J/$mm^2$) and a system-wide wall-plug efficiency of 75%. For an industrial-scale representative coil (1000 mm width, 3 mm thickness), the total electrical energy requirement is determined as 34.9 kWh/ton.

**Table 5-1** Utility Consumption Comparison per Metric Ton of Steel.

| *Utility Type* | *Conventional CPL Baseline* | *Laser Cleaning (500 W)* |
|---|---|---|
| ***Electricity (Direct)*** | 8.0 kWh | 34.9 kWh |
| ***Natural Gas*** | 2.1 $Sm^3$ (22.34 kWh) | **0** |
| ***Total Energy Equivalent*** | **30.34 kWh** | **34.9 kWh** |

As illustrated in Table 5.1, the 500 W laser system is already operating within the same order of magnitude as the total energy requirement of chemical pickling. The downward trendline suggests that as laser power increases and thermodynamic coupling improves, the total energy intensity of laser cleaning will fall below the CPL baseline. Beyond numerical parity, this transition represents a strategic shift toward decarbonization; whereas CPLs are dependent on fossil fuels, a laser system can be powered entirely by renewable electricity, enabling a zero-emission surface treatment process.

## 5.3 Comparative Surface Integrity Assessment of Pickled and Laser-Cleaned Steel

Although the energy comparison presented in the previous sections indicates that laser-based oxide removal may offer a significant advantage over conventional pickling, the performance of the cleaned surface remains a critical factor for industrial applicability. In continuous flat steel processing, successful oxide removal alone is not sufficient; the cleaned surface must also preserve the required surface quality, near-surface microstructural integrity, and mechanical uniformity for subsequent processing steps. Therefore, in addition to the energy-based evaluation, a comparative surface integrity assessment was carried out between conventionally pickled and laser-cleaned hot-rolled steel samples.

For this purpose, representative samples were taken from two different products processed by conventional CPL pickling and laser cleaning, respectively. The comparative assessment included surface roughness measurements, cross-sectional metallographic examination by SEM, and near-surface hardness measurements.

The surface roughness profiles of the conventionally pickled and laser-cleaned samples are shown in Figure 5-1, and the corresponding roughness parameters are summarized in Table 5-2. The results clearly indicate that laser-based oxide removal produced a rougher surface compared with conventional acid pickling. In particular, the measured $R_a$ value increased from 1.269 µm for the CPL baseline sample to 3.700 µm for the laser-cleaned sample, corresponding to nearly a threefold increase. Similarly, the $R_z$ value increased from 9.899 µm to 23.626 µm, indicating a higher peak-to-valley surface amplitude after laser cleaning. On the other hand, the $R_{Pc}$ value remained relatively comparable, suggesting that the main difference between

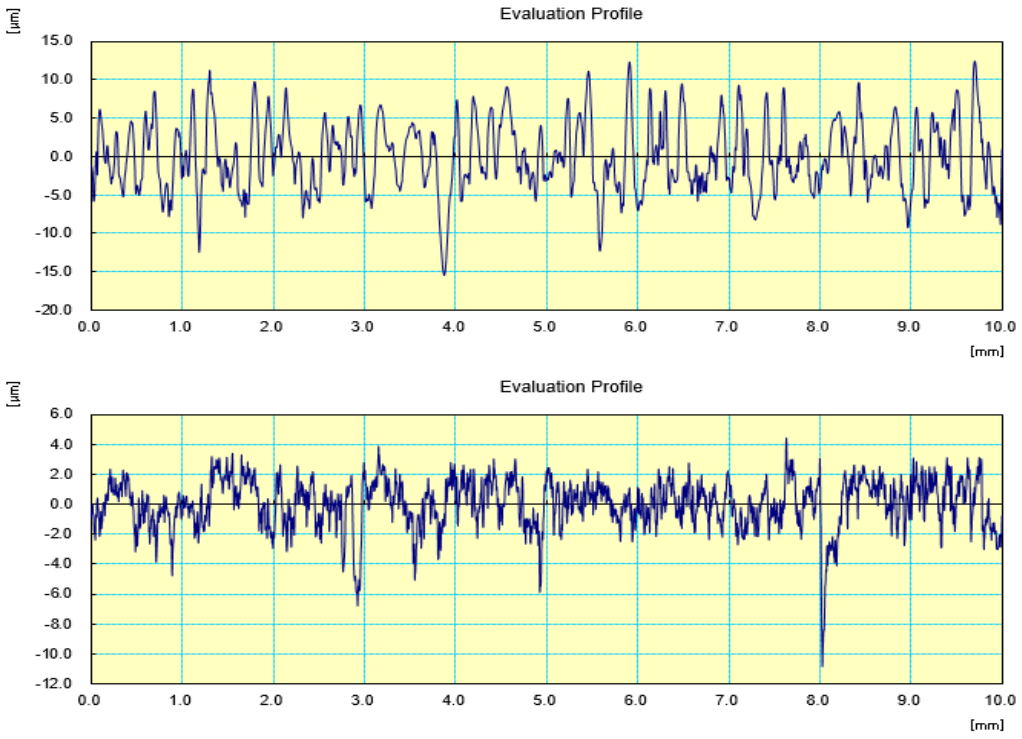


**Figure 5-1** Surface roughness profiles of the steel samples: laser-cleaned surface on the top and conventionally pickled surface on the bottom, illustrating the increased surface roughness generated by laser-based oxide removal.

the two surfaces was not necessarily the number of surface peaks, but rather the amplitude and severity of the surface irregularities.

**Table 5-2** Surface roughness measurements of conventionally pickled and laser-cleaned steel samples.

| | ***Conventional CPL Baseline*** | ***Laser Cleaning (500 W)*** |
|---|---|---|
| $R_a$ | 1.269 μm | 3.700 μm |
| $R_z$ | 9.899 μm | **23.626 μm** |
| $R_{Pc}$ | **46.03 /cm** | **40.50 /cm** |

From an application perspective, this increase in surface roughness may have both positive and negative implications. For hot-rolled products that are directly coated after oxide removal, such as galvanized hot-rolled coils, a rougher surface may potentially improve coating adhesion by increasing the effective surface area and mechanical anchoring of the coating. However, for products that will undergo subsequent cold rolling, excessive surface roughness may be detrimental. Pronounced surface irregularities may promote non-uniform deformation during cold rolling and may lead to localized stress concentration under rolling loads. Therefore, while the increased roughness generated by laser cleaning may be beneficial for certain direct-coating applications, it may create additional risks for product routes involving further cold reduction.

To further evaluate whether the increased roughness was accompanied by any near-surface microstructural modification, cross-sectional SEM examinations were performed on both the laser-cleaned and conventionally pickled samples. The SEM micrographs of the laser-cleaned sample are presented in Figure 5-2, while the conventionally pickled reference sample is shown in Figure 5-3.

As shown in Figure 5-2, the laser-cleaned sample exhibited a distinguishable laser-affected near-surface region beneath the cleaned surface. The thickness of this modified region was measured to vary approximately between 10 and 22 µm. In this region, the conventional ferritic grain structure observed in the bulk material was no longer clearly distinguishable, indicating that the laser treatment did not only remove the oxide scale but also locally affected the underlying steel substrate. In contrast, the conventionally pickled sample shown in Figure 5-3 did not exhibit such a modified near-surface layer. The grain structure was observed to continue uniformly up to the surface, confirming that acid pickling removed the oxide scale without producing a visible microstructural alteration in the base metal..

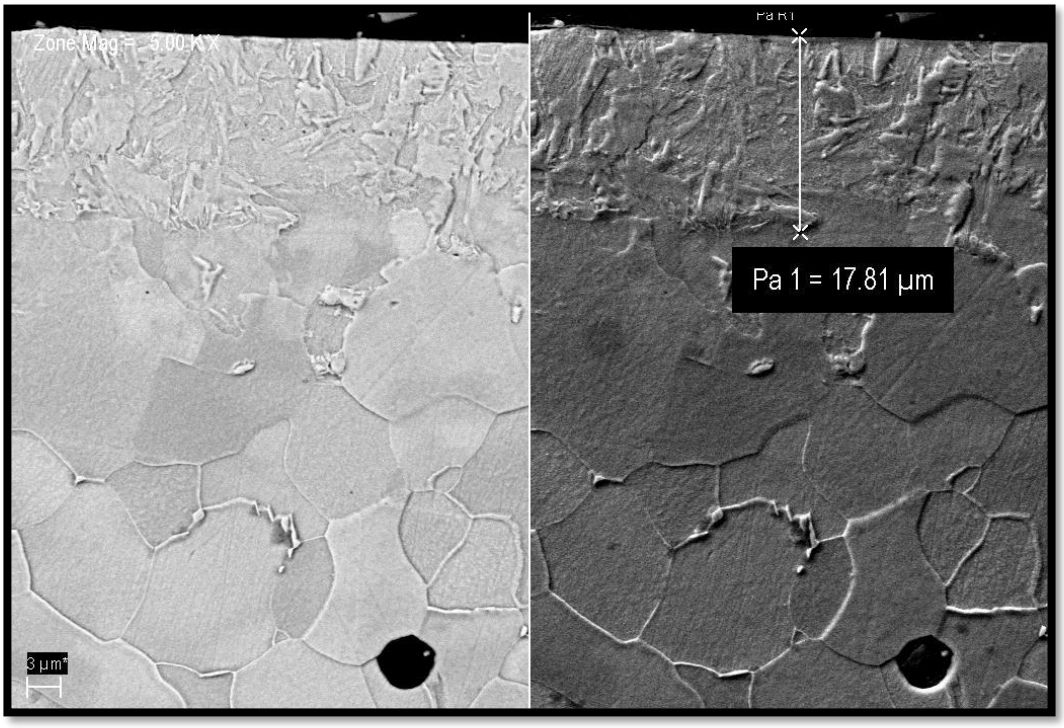


**Figure 5-2** Cross-sectional SEM micrographs of the steel sample exposed to 500 W laser power: backscattered electron (BSE) image on the left and secondary electron (SE) image on the right, indicating the measured laser-affected near-surface region.

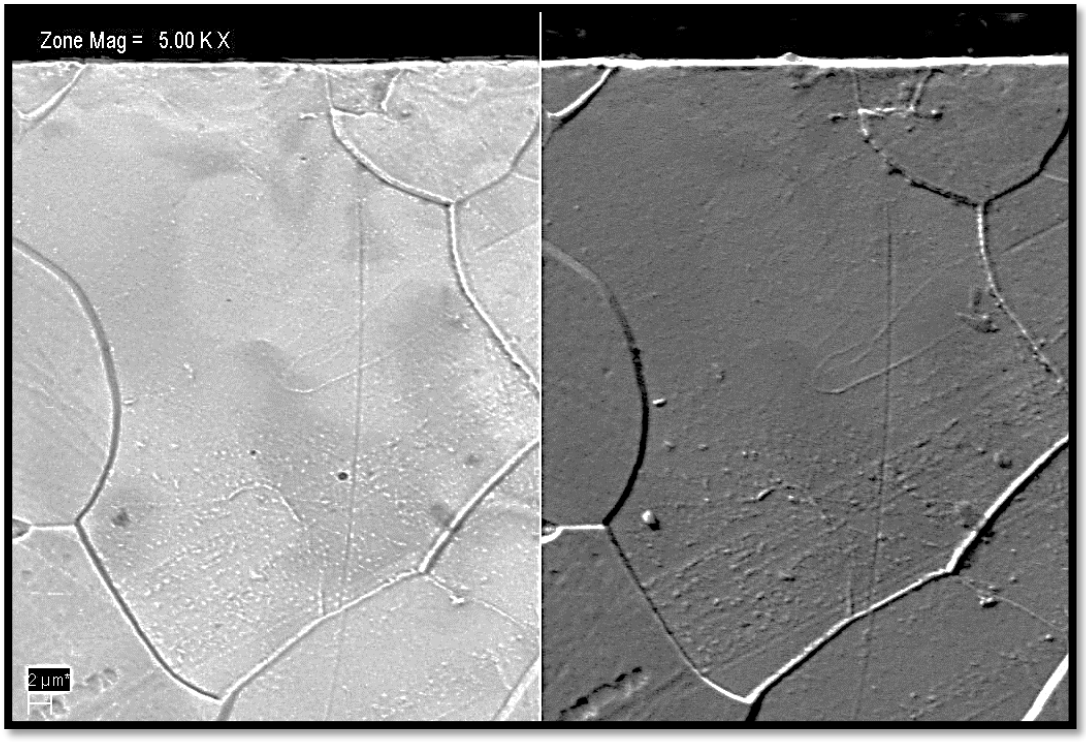


**Figure 5-3** Cross-sectional SEM micrographs of the conventionally pickled steel sample: BSE image on the left and SE image on the right, showing the absence of a laser-affected near-surface region.

The metallographic observations suggest that the laser-affected region may have formed as a result of rapid heating and cooling during laser irradiation. Based on the observed morphology, the formation of acicular ferrite-like structures is considered possible; however, this interpretation requires further confirmation by phase-sensitive characterization techniques such as EBSD or higher-resolution microstructural analysis. Therefore, the observed layer should be interpreted as a laser-affected near-surface region rather than being assigned to a definitive phase at this stage.

Near-surface hardness measurements were also conducted to assess the mechanical significance of this modified region. The corresponding microhardness profiles are presented in Figure 5-4.

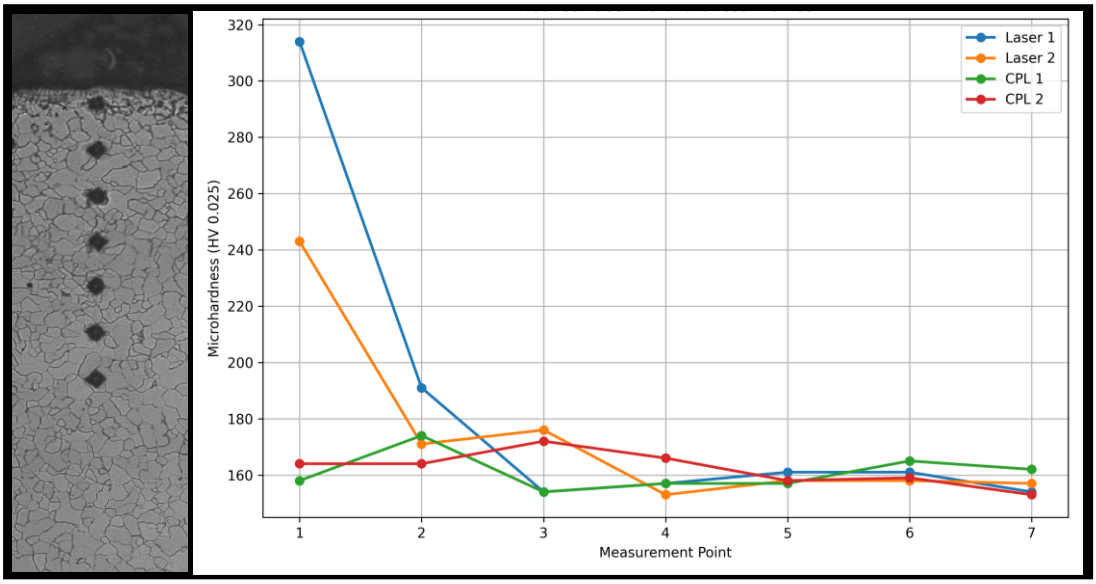


**Figure 5-4** Representative image of near-surface microhardness indentations on the left and corresponding microhardness profiles of laser-cleaned and conventionally pickled steel samples on the right (HV 0.025).

As shown in Figure 5-4, the conventionally pickled samples exhibited a relatively uniform hardness distribution throughout the measured points, with values generally remaining in the range of approximately 150–175 HV 0.025. In contrast, the laser-cleaned samples showed a pronounced hardness increase at the first measurement point, corresponding to the region closest to the surface. The hardness values at this point reached 314 HV 0.025 for Laser 1 and 243 HV 0.025 for Laser 2, whereas the CPL samples remained at 158–164 HV 0.025. After the first few measurement points, the hardness values of the laser-cleaned samples approached those of the CPL samples, suggesting that the laser-induced modification was mainly limited to the near-surface region. This localized hardness increase is consistent with the SEM observations and supports the presence of laser-induced microstructural modification beneath the cleaned surface.

From an industrial perspective, the formation of a harder and microstructurally modified near-surface region may be critical for products subjected to subsequent

cold rolling. Local variations in hardness and microstructure can promote non-uniform deformation under rolling loads and may increase the risk of localized stress concentration, surface defects, tearing, or strip breakage. Therefore, although laser cleaning demonstrated promising energy-related advantages, the observed increase in surface roughness, near-surface microstructural modification, and localized hardness increase indicate that surface integrity must be carefully considered before industrial implementation.

It should be noted that these findings were obtained under the selected laser-cleaning condition of 500 W laser power, 20 kHz pulse frequency, and 15 mJ pulse energy. Since these parameters directly affect heat input, thermal accumulation, ablation efficiency, and substrate modification, further laser parameter optimization is necessary. Reducing the heat input while maintaining sufficient oxide removal efficiency should be considered a key objective in future studies. In particular, minimizing or eliminating the laser-affected near-surface region is essential for enabling the safe application of laser cleaning in product routes involving subsequent cold rolling. However, for directly coated hot-rolled products, the higher roughness generated by laser cleaning may still provide a potential advantage and should be further investigated through coating adhesion and galvanizing performance studies.

# CHAPTER 6

## CONCLUSIONS AND FUTURE RECOMMENDATIONS

This study has systematically investigated the feasibility of laser-based descaling as a sustainable alternative to conventional acid pickling in hot-rolled flat steel production. By integrating detailed material characterization, experimental process optimization, and energy analysis, a comprehensive understanding of the laser–oxide interaction and its industrial applicability has been established.

The characterization of the oxide layer revealed that the scale formed on hot-rolled steels exhibits significant variability in both thickness and phase composition, strongly influenced by processing parameters such as cooling rate, coiling temperature, and alloy chemistry. The oxide layer was found to predominantly consist of magnetite, with minor fractions of hematite and wüstite. Additionally, a consistent transverse thickness gradient was observed across the coil width, with the center region representing the most critical "worst-case" scenario for descaling. These findings highlight the necessity of a material-specific and condition-dependent approach for process design.

Optical characterization demonstrated that magnetite exhibits strong absorption in the near-infrared (NIR) region, whereas hematite shows relatively lower absorption at these wavelengths. Based on this analysis, a wavelength of 1070 nm was identified as the most suitable for efficient energy coupling with the oxide layer. This selection provided a critical foundation for optimizing the laser descaling process and ensured effective interaction with the dominant oxide phase.

The experimental investigations revealed a clear distinction between continuous-wave (CW) and pulsed-wave (PW) laser operation modes. CW processing was found to be thermodynamically unsuitable for descaling, as continuous heat input led to excessive thermal accumulation, promoting secondary oxidation and even increasing

the oxide layer thickness. In contrast, PW laser operation enabled precise thermal confinement, allowing for efficient oxide removal without damaging the underlying steel substrate.

Through systematic parameter optimization, a clear ablation mechanism was identified, consisting of distinct stages ranging from initial cracking to complete descaling. The optimal operational window for complete oxide removal was successfully established, with higher laser power levels significantly expanding the processing envelope. Notably, the results demonstrated that increasing laser power not only enhances processing speed but also improves energy efficiency, reducing the specific energy requirement from 2.00 J/mm² at low power to 1.11 J/mm² at higher power levels.

From an industrial perspective, the feasibility analysis indicated that laser-based descaling is already operating within the same order of magnitude in terms of total energy consumption compared to conventional pickling processes. While the current energy requirement of the laser system is slightly higher, the absence of chemical consumption, elimination of acid regeneration systems, and compatibility with renewable energy sources present a significant advantage. Furthermore, the non-chemical nature of the process eliminates issues such as tramp element accumulation and surface contamination, offering a cleaner and more controllable surface preparation route. However, the comparative surface integrity assessment indicated that laser-based oxide removal should not be evaluated solely in terms of cleaning efficiency and energy consumption. Compared with the conventionally pickled sample, the laser-cleaned surface exhibited higher roughness, a laser-affected near-surface region with a thickness of approximately 10–22 µm, and a localized increase in surface hardness. These findings suggest that further optimization of laser parameters is required to minimize thermal effects on the substrate, particularly for products intended for subsequent cold rolling

Overall, the findings of this study demonstrate that laser-based descaling is not only technically viable but also represents a highly promising pathway toward sustainable

steel production. As laser technologies continue to advance and system efficiencies improve, it is expected that this approach will surpass conventional methods both in energy performance and environmental impact.

In conclusion, the transition from chemical-based pickling to laser-based descaling offers a compelling opportunity for the steel industry to reduce its environmental footprint while maintaining high product quality and process efficiency. However, to further strengthen the industrial applicability of this technology, additional investigations at higher laser power levels are required to fully define the operational limits and scalability of the process. Moreover, hybrid approaches integrating laser systems with conventional pickling lines may provide a practical intermediate solution by significantly reducing acid consumption while maintaining process reliability. Such integration strategies could serve as a transitional pathway toward fully chemical-free surface treatment systems. Future work should therefore focus on high-power system optimization, process integration in continuous production lines, and further improvements in overall energy efficiency to fully realize the potential of laser-based descaling within the green transition of the steel industry.

# REFERENCES


[1] R. J. Holmes, Y. Lu, and L. Lu, “Chapter 1 - Introduction: Overview of the global iron ore industry,” in *Iron Ore (Second Edition)*, Second Edition., L. Lu, Ed., in Woodhead Publishing Series in Metals and Surface Engineering. , Woodhead Publishing, 2022, pp. 1–56. doi: https://doi.org/10.1016/B978-0-12-820226-5.00023-9.

[2] H. K. D. H. Bhadeshia and R. W. K. Honeycombe, “1 - Iron and its interstitial solutions,” in *Steels (Fifth Edition)*, Fifth Edition., H. K. D. H. Bhadeshia and R. W. K. Honeycombe, Eds., Butterworth-Heinemann, 2024, pp. 1–22. doi: https://doi.org/10.1016/B978-0-44-318491-8.00007-1.

[3] H. K. D. H. Bhadeshia and R. W. K. Honeycombe, “2 - Strengthening of iron and its alloys,” in *Steels (Fifth Edition)*, Fifth Edition., H. K. D. H. Bhadeshia and R. W. K. Honeycombe, Eds., Butterworth-Heinemann, 2024, pp. 23–60. doi: https://doi.org/10.1016/B978-0-44-318491-8.00008-3.

[4] M. Huang, B. He, Y. Li, and M. Wang, “Chapter One - General introduction,” in *High Strength Steels*, M. Huang, B. He, Y. Li, and M. Wang, Eds., in Acta Materialia Book Series. , Elsevier, 2025, pp. 1–41. doi: https://doi.org/10.1016/B978-0-443-15898-8.00002-4.

[5] K.-E. Thelning, “5 - Heat treatment—general,” in *Steel and its Heat Treatment (Second Edition)*, Second Edition., K.-E. Thelning, Ed., Butterworth-Heinemann, 1984, pp. 207–318. doi: https://doi.org/10.1016/B978-0-408-01424-3.50009-1.

[6] K.-E. Thelning, “1 - Fundamental metallographic concepts,” in *Steel and its Heat Treatment (Second Edition)*, Second Edition., K.-E. Thelning, Ed., Butterworth-Heinemann, 1984, pp. 1–47. doi: https://doi.org/10.1016/B978-0-408-01424-3.50005-4.

[7] M. Huang, B. He, Y. Li, and M. Wang, “Chapter Three - Dual-phase steel,” in *High Strength Steels*, M. Huang, B. He, Y. Li, and M. Wang, Eds., Elsevier, 2025, pp. 71–94. doi: https://doi.org/10.1016/B978-0-443-15898-8.00006-1.

[8] N. Fonstein, “7 - Dual-phase steels in *Automotive Steels*, R. Rana and S. B. Singh, Eds., Woodhead Publishing, 2017, pp. 169–216. doi: https://doi.org/10.1016/B978-0-08-100638-2.00007-9.

[9] E. Çelikses, İ. Yelek, M. Özdemir, and T. Yalçinkaya, “Microstructure Based Analysis of Plasticity and Failure of Dual Phase Steels,” *Procedia Structural Integrity*, vol. 68, pp. 1045–1050, 2025, doi: https://doi.org/10.1016/j.prostr.2025.06.168.

[10] D. WHITE, “CHAPTER 7 - Standards,” in *How to Find Out in Iron and Steel*, D. WHITE, Ed., in The Commonwealth and International Library: Libraries and Technical Information Division. , Pergamon, 1970, pp. 118–133. doi: https://doi.org/10.1016/B978-0-08-015790-0.50009-1.

[11] B. Björkman and C. Samuelsson, “Chapter 6 - Recycling of Steel,” in *Handbook of Recycling*, E. Worrell and M. A. Reuter, Eds., Boston: Elsevier, 2014, pp. 65–83. doi: https://doi.org/10.1016/B978-0-12-396459-5.00006-4.

[12] D. Raabe, “The Materials Science behind Sustainable Metals and Alloys,” *Chem Rev*, vol. 123, no. 5, pp. 2436–2608, Mar. 2023, doi: 10.1021/acs.chemrev.2c00799.

[13] A. S. M. H. Committee, *Properties and Selection: Irons, Steels, and High-Performance Alloys*. ASM International, 1990. doi: 10.31399/asm.hb.v01.9781627081610.

[14] H. Koohestani and M. Majidi, “A review on green steel; introduction, benefits and challenges of the steelmaking industry,” *Ironmaking & Steelmaking*, vol. 0, no. 0, p. 03019233251345982, doi: 10.1177/03019233251345982.

[15] S. Yao, H. Zhu, S. Zhang, H. Chang, and H. Wang, “Green steel: The future path towards sustainable automotive manufacturing,” *Resour Conserv Recycl*, vol. 200, p. 107319, 2024, doi: https://doi.org/10.1016/j.resconrec.2023.107319.

[16] S. Seetharaman, “Chapter 1 - Process Metallurgy—An Argosy Through Time,” in *Treatise on Process Metallurgy*, S. Seetharaman, Ed., Boston: Elsevier, 2014, pp. 1–13. doi: https://doi.org/10.1016/B978-0-08-096986-2.00026-6.

[17] V. Smil, “Iron and Steel Before the Eighteenth Century,” *Still the Iron Age*, pp. 1–17, 2016, doi: 10.1016/B978-0-12-804233-5.00001-4.

[18] V. Smil, “Chapter 3 - Iron and Steel Before WW I, 1850–1914: The Age of Affordable Steel,” in *Still the Iron Age*, V. Smil, Ed., Boston: Butterworth-Heinemann, 2016, pp. 35–64. doi: https://doi.org/10.1016/B978-0-12-804233-5.00003-8.

[19] V. Smil, “Chapter 5 - Modern Ironmaking and Steelmaking: Furnaces, Processes, and Casting,” in *Still the Iron Age*, V. Smil, Ed., Boston: Butterworth-Heinemann, 2016, pp. 87–114. doi: https://doi.org/10.1016/B978-0-12-804233-5.00005-1.

[20] P. Wang *et al.*, “Efficiency stagnation in global steel production urges joint supply- and demand-side mitigation efforts,” *Nat Commun*, vol. 12, no. 1, p. 2066, 2021, doi: 10.1038/s41467-021-22245-6.

[21] C. A. "Smith, “Review of raw materials for steelmaking,” vol. 209:12, 1981, doi: https://doi.org/.

[22] R. R. Wang, Y. Q. Zhao, A. Babich, D. Senk, and X. Y. Fan, “Hydrogen direct reduction (H-DR) in steel industry—An overview of challenges and opportunities,” *J Clean Prod*, vol. 329, p. 129797, 2021, doi: https://doi.org/10.1016/j.jclepro.2021.129797.

[23] J. Kim *et al.*, “Decarbonizing the iron and steel industry: A systematic review of sociotechnical systems, technological innovations, and policy options,” *Energy Res Soc Sci*, vol. 89, p. 102565, 2022, doi: https://doi.org/10.1016/j.erss.2022.102565.

[24] R. B. G. Yeo, A. G. Melville, P. E. Repas, and J. M. Gray, “Properties and Control of Hot-Rolled Steels,” *JOM*, vol. 20, no. 6, pp. 33–43, 1968, doi: 10.1007/BF03378721.

[25] W. F. Kladnig, “A review of steel pickling and acid regeneration an environmental contribution,” *International Journal of Materials and Product Technology*, vol. 19, no. 6, pp. 550–561, Jan. 2003, doi: 10.1504/IJMPT.2003.003471.

[26] N. B. Dülger *et al.*, “Effect of deformation in C67 steel on spheroidization temperature and duration,” *J Phys Conf Ser*, vol. 3035, no. 1, p. 012018, 2025, doi: 10.1088/1742-6596/3035/1/012018.

[27] V. Kuklík and J. Kudláček, “5 - Morphology of hot-dip galvanized coatings,” in *Hot-Dip Galvanizing of Steel Structures*, V. Kuklík and J. Kudláček, Eds., Boston: Butterworth-Heinemann, 2016, pp. 41–65. doi: https://doi.org/10.1016/B978-0-08-100753-2.00005-7.

[28] Md. Z. Islam, “Europe’s policy transition toward green steel development: Prospective and challenges,” *Int J Green Energy*, vol. 22, no. 2, pp. 288–306, Jan. 2025, doi: 10.1080/15435075.2024.2413684.

[29] A. N. Canat and C. Özkan, “Supplying hydrogen for green steel through renewable energy sources: A case study of Turkiye,” *J Clean Prod*, vol. 450, p. 141961, 2024, doi: https://doi.org/10.1016/j.jclepro.2024.141961.

[30] M. Pérez-Fortes, J. A. Moya, K. Vatopoulos, and E. Tzimas, “CO2 Capture and Utilization in Cement and Iron and Steel Industries,” *Energy Procedia*, vol. 63, pp. 6534–6543, 2014, doi: https://doi.org/10.1016/j.egypro.2014.11.689.

[31] Y. Zhang, L. Yu, K. Cui, H. Wang, and T. Fu, “Carbon capture and storage technology by steel-making slags: Recent progress and future challenges,” *Chemical Engineering Journal*, vol. 455, p. 140552, 2023, doi: https://doi.org/10.1016/j.cej.2022.140552.

[32] San Roman Alerigi, D. P., Mutairi, S., Batarseh, S., & Assiri, W. (2022, October). *Principles and advantages of high-power lasers for descaling surface equipment*. Paper presented at the SPE Annual Technical Conference and Exhibition, Houston, Texas, USA. https://doi.org/10.2118/209977-MS

[33] Schlüter, H., Zwick, A., Aden, M., Uhlig, G., Wissenbach, K., & Beyer, E. (1994). Descaling of austenitic steels by laser radiation. In *ICALEO '94: Proceedings of the Laser Materials Processing Conference* (pp. 95-104). ASME. https://doi.org/10.2351/1.5058876

[34] Guo, H., Martukanitz, R., & DebRoy, T. (2004). Laser assisted cleaning of oxide films on SUS409 stainless steel. *Journal of Laser Applications*, 16(4), 236-241. https://doi.org/10.2351/1.1809639

[35] Lim, H., & Kim, D. (2004). Laser-assisted chemical cleaning for oxide-scale removal from carbon steel surfaces. *Journal of Laser Applications*, 16(1), 25-29. https://doi.org/10.2351/1.1642631

[36] Zhang, Z., Zhang, J., Wang, Y., Liang, H., Liu, Y., Zhao, S., Li, X., & Lin, X. (2017). Surface cleaning of hot-rolled sheet steel by laser ablation of oxide layer

using a 100-ns high-repetition frequency pulsed laser. *Optical Engineering*, 56(11), 116114. https://doi.org/10.1117/1.OE.56.11.116114

[37] Zhurba, D. V., Zhurba, V. M., Veiko, V. P., & Puisha, A. E. (2024). Investigation of the process of laser descaling of mill metal. *Photonics Russia*, 18(6), 436-449. https://doi.org/10.22184/1993-7296.FRos.2024.18.6.436.449

[38] Chen, R. Y., & Yuen, W. Y. D. (2001). Oxide-scale structures formed on commercial hot-rolled steel strip and their formation mechanisms. *Oxidation of Metals*, 56(1-2), 89-118. https://doi.org/10.1023/A:1010395419981

[39] Jia, Q., Jiang, X., Wu, C., Chen, J., Zhu, X., Liu, Y., & Su, X. (2025). Effect of Si on Mechanical Properties and Oxide Film Formation of AFA Alloy at Low Oxygen Pressure. *Coatings*, 15(4), 602. https://doi.org/10.3390/coatings15050602

[40] Yang, Y.-L., Yang, C.-H., Lin, S.-N., Chen, C.-H., & Tsai, W.-T. (2008). Effects of Si and its content on the scale formation on hot-rolled steel strips. *Materials Chemistry and Physics*, 112(2), 566-571. https://doi.org/10.1016/j.matchemphys.2008.06.021

[41] Abuluwefa, H., Guthrie, R. I. L., & Yue, S. (1996). The effect of carbon content on the oxidation kinetics of steels. *Metallurgical and Materials Transactions A*, 27(6), 1633-1640. https://doi.org/10.1007/BF02649833

[42] Chen, R. Y., & Yuen, W. Y. D. (2003). Review of the high-temperature oxidation of iron and carbon steels in air or oxygen. *Oxidation of Metals*, 59(5-6), 433-468. https://doi.org/10.1023/A:1023685905159

[43] Zhang, W., Wang, C., Wu, Q., Yan, F., Zhu, G., & Wang, J. (2025). Oxide Removal Mechanism and Process Optimization During Integrated Pulsed-Continuous Laser Cleaning of Q235B Carbon Steel. *Materials*, 18(6), 1247

[44] Erdoğan, M., Karakaya, E., Aras, M. S., Karagül, S. Ç., Ersoy, M. K., Öztürk, A., & Karakaya, İ. (2018). Removal of Trace Amounts of Copper from Concentrated

Hydrochloric Acid Solutions. *International Journal of Electrochemical Science*, 13(11), 10934-10947. https://doi.org/10.20964/2018.11.75

[45] BOTAŞ. (2024). *Doğal Gaz Birim Dönüşüm Tabloları ve Enerji Değerleri.* Boru Hatları ile Petrol Taşıma A.Ş., Ankara, Türkiye.